

INVARIANT MANIFOLDS AND GLOBAL BIFURCATIONS TO FIND MULTIPLE WAVE SOLUTIONS IN A REACTION-DIFFUSION SYSTEM

EDGARDO VILLAR-SEPÚLVEDA*, PABLO AGUIRRE**, AND VÍCTOR F. BREÑA-MEDINA†

ABSTRACT. A thorough analysis is performed to find traveling waves in a qualitative reaction-diffusion system inspired by a predator-prey model. We provide rigorous results coming from a standard local stability analysis, numerical bifurcation analysis, and relevant computations of invariant manifolds to exhibit homoclinic and heteroclinic connections, and periodic orbits in the associated traveling wave system with four components. In so doing, we present and describe a zoo of different traveling wave solutions. In addition, homoclinic chaos is manifested via both saddle-focus and focus-focus bifurcations as well as a Belyakov point. An actual computation of global invariant manifolds near a focus-focus homoclinic bifurcation is also presented to unravel a multiplicity of wave solutions in the model.

1. INTRODUCTION

Invariant manifold analysis and global bifurcations are among the *avant garde* of research topics in nonlinear dynamical systems. From the seminal works of L. P. Shilnikov [1, 48, 49] onwards, global bifurcations and invariant manifolds have gained a lot of attention from the dynamical systems community; see, for instance, the survey by Guckenheimer *et al.* [20], and references therein for different high-profile scenarios including slow-fast dynamics, homoclinic orbits in high-dimensions, and traveling waves phenomena. Geometrically, global bifurcations of vector fields are associated with invariant manifolds of equilibria and/or periodic orbits, quasiperiodic invariant tori [21, 23, 30], and slow manifolds of systems with multiple timescales [36, 37]. Perturbations of the system parameters typically cause global rearrangements of such invariant manifolds, leading to reorganizations of the overall dynamics in the phase space. These can bring forth the creation/destruction of homoclinic and heteroclinic connections, and the (dis)appearance of attracting (repelling) invariant objects, including periodic orbits and even chaotic dynamics [30, 50]. Hence, global invariant manifolds emerge as the “building blocks” of a dynamical system, i.e., those essential objects help to explain how the overall “architecture” of phase space is organized.

One of the applications of invariant manifold analysis lies on the existence of traveling wave solutions for reaction-diffusion equations. This kind of solution emerges as a suitable mathematical approach to describe wave-like spatial movement of populations, transport of nutrients and biological substances, etc.; see, for instance, the textbooks [39, 38] and references therein. Indeed, traveling waves represent spatiotemporal transitions from one homogeneous steady state to another one, or to itself [23, 32, 38, 46, 53]. Typically, the mathematical analysis to find this kind of solution involves the reduction of the reaction-diffusion equations into a system of ordinary differential equations in which one searches for heteroclinic or homoclinic orbits. However, the problem of obtaining these connecting orbits and

2020 *Mathematics Subject Classification.* 37N25, 35C07, 92D40, 37C29, 37D10, 37G20, 35Q92.

Key words and phrases. Homoclinic and heteroclinic orbits, traveling waves, invariant manifolds, bifurcation analysis.

EVS was partially funded by Programa de Incentivo a la Iniciación Científica PIIC DGIIP-UTFSM and his work was carried out at the Departamento de Matemática, Universidad Técnica Federico Santa María. EVS and PA were partially funded by Proyecto Interno UTFSM PI-LI-19-06. PA also thanks Proyecto Basal CMM Universidad de Chile. VFBM thanks the financial support by Asociación Mexicana de Cultura A.C..

associated global (un)stable manifolds is a challenging task. With the exception of a few concrete examples (see, e.g., [23]), in general, there are no analytical expressions for homoclinic orbits or non-local normal forms. Hence, it is frequent to make use of reductions to Poincaré maps in suitable cross sections, center manifold reductions and other analytical approaches to prove the existence of intersecting invariant manifolds giving rise to homoclinic and heteroclinic connections; see [15, 24, 25, 35, 43, 51, 54] for different examples.

The purpose of this paper is to establish the existence of traveling wave solutions for the following reaction-diffusion system:

$$\begin{cases} u_t = D_1 u_{xx} + u(u - m)(1 - u)(u + v) - \alpha uv, \\ v_t = D_2 v_{xx} + \beta uv - \gamma v(u + v), \end{cases} \quad (1)$$

where short notation is used for partial derivatives: $w_t = \partial w / \partial t$ and $w_{xx} = \partial^2 w / \partial x^2$. In (1), $u = u(x, t)$ and $v = v(x, t)$ are the unknown variables as functions of the spatial variable $x \in [-L, L]$ and time $t > 0$. The characteristic length of the state variables interaction domain is assumed to be such that $L \rightarrow \infty$ as traveling waves solutions are known to arise in systems as (1) (see e.g. [9, 25, 31, 34]); diffusion rates $D_1, D_2 > 0$ correspond to mobilities which are a measure of the spatial dispersion efficiency of u and v , respectively [38].

System (1) is inspired by a predator-prey model from [5] accounting for strong Allee effect on prey and ratio-dependent functional response. However, the main purpose of (1) is not to duplicate exactly quantitative aspects of the predator-prey interactions from the model it is inspired by. Rather, (1) is meant as an elementary, minimal model in which one can display the sorts of mathematical relations between variables underlying the connections in [5]. Hence, we refrain from calling u and v as the prey and predators, respectively, in order to avoid misunderstandings with the interpretation of results of the conceptual model (1). We note that our approach to (1) is similar to that of other qualitative models in biology such as the celebrated Fitzhugh-Nagumo model for action potentials in neurons [38], or the Izhikevich [26], Hindmarsh-Rose [47] and the canonical Ermentrout-Kopell [17] models. Indeed, while these abstract models are constructed less closely to physiological features and thus less interpretable, they succeed in portray diverse essential neuronal behaviors with just the minimal mathematical ingredients (see [16] and references therein).

With a strategic combination of numerical methods for invariant manifolds and bifurcation theory, we find the traveling wave solutions identifying each of them as a specific heteroclinic/homoclinic connection or a periodic orbit in the four-dimensional phase space of the associated ODEs. We classify these solutions into 12 different classes depending on the topological type of the associated orbit. We also determine conditions on the model parameters so that there is such a particular kind of solution and identify homoclinic chaotic dynamics as one of the sources of complicated behavior.

Today, homoclinic and heteroclinic orbits can readily be computed and continued with software packages like AUTO [14] (with its extension HOMCONT [10]) and MATCONT [12] with high accuracy. In addition, one can locate homoclinic and heteroclinic connections as intersections of global invariant manifolds. This can be achieved by direct computation and inspection of the manifolds [3, 6], or by setting additional techniques such as Lin's method [27]. While one-dimensional invariant manifolds can be approximated using straightforward integration from a given initial condition, the computation of higher-dimensional manifolds of equilibria and periodic orbits requires advanced numerical techniques. The two-dimensional global manifolds in this paper are computed as families of orbit segments, which can be obtained as solutions of a suitable boundary value problem (BVP), irrespective of the vector field undergoing a homoclinic or heteroclinic bifurcation. This allows us to make use of AUTO to implement and solve the BVP; then, the manifold is "built up" by continuation of the respective orbit segments [28, 29]; see also [4, 2, 6, 20] for further details and applications. Moreover, while some works have dealt with traveling waves associated with three-dimensional vector fields [33, 51, 54], our

problem involves a four-dimensional phase space, which is a major challenge. Although the human brain is efficient when capturing depth in flat images of 3-dimensional objects, this ability is not as effective in higher dimensions [11, 40]. When trying to visualize objects in a 4D phase space —such as invariant manifolds—, standard projections may give rise to false intersections between them. These artifacts due to projections must be detected and differentiated from real intersections to ensure or discard the existence of homoclinic or heteroclinic connections. To do so, we make extensive use of dynamical systems theory and topological arguments to justify our findings. In addition, wave trains are found as periodic orbits originating via Hopf bifurcations; see also [15, 24, 25, 35, 42] for other uses of this theoretical argument.

This paper is organized as follows: Figure 2 presents some definitions, notation and preliminary results. Local stability analysis of steady states is included in Figure 3, while a bifurcation analysis is presented in Figure 4. Wave pulses, wave trains and wave fronts are discussed in Figure ??, respectively. Figure 8 presents a description of the multiple wave fronts found near a focus-focus homoclinic bifurcation. Figure 9 discusses the influence of the propagation speed and the diffusion ratio on the occurrence of the different wave pulses. Figure 10 analyzes the existence of traveling fronts in two invariant planes. Finally, Figure 11 presents a summary and discussion of the main results.

2. PRELIMINARIES AND FIRST EXAMPLES

For future convenience, the first step to study traveling wave solutions in (1) is to make a time rescaling and a change of parameters given, respectively, by

$$t \rightarrow D_2 t, \quad (d, s, b, g, a, m) = \left(\frac{D_1}{D_2}, \frac{1}{D_2}, s\beta, s\gamma, s\alpha, m \right) \in \mathbb{R}_+^5 \times]0, 1[.$$

Thus, we can write system (1) equivalently as

$$(2) \quad \begin{cases} u_t = du_{xx} + su(u-m)(1-u)(u+v) - auv; \\ v_t = v_{xx} + buv - gv(u+v). \end{cases}$$

Here, $d = D_1/D_2$ represents the ratio of diffusion rates of u and v , respectively, and appears as an explicit parameter in (2). If $d > 1$ (resp. $d < 1$), u is more (resp. less) efficient to disperse in space compared to v .

We now consider the so-called wave variable $z = x + ct$, where $c > 0$ is the wave speed, and we look for solutions of (2) of the form $U(z) = u(x, t)$, $V(z) = v(x, t)$. Applying the chain rule and substituting this into (2), we obtain the following set of second order ordinary differential equations

$$(3) \quad \begin{cases} c \frac{dU}{dz} = d \frac{d^2 U}{dz^2} + sU(U-m)(1-U)(U+V) - aUV; \\ c \frac{dV}{dz} = \frac{d^2 V}{dz^2} + bUV - gV(U+V). \end{cases}$$

Naming the auxiliary variables $W = dU/dz$ and $R = dV/dz$, system (3) can be expressed equivalently as the vector field

$$(4) \quad X : \begin{cases} \frac{dU}{dz} = W, \\ \frac{dV}{dz} = R, \\ \frac{dW}{dz} = \frac{1}{d} (cW - sU(U-m)(1-U)(U+V) + aUV), \\ \frac{dR}{dz} = cR - bUV + gV(U+V). \end{cases}$$

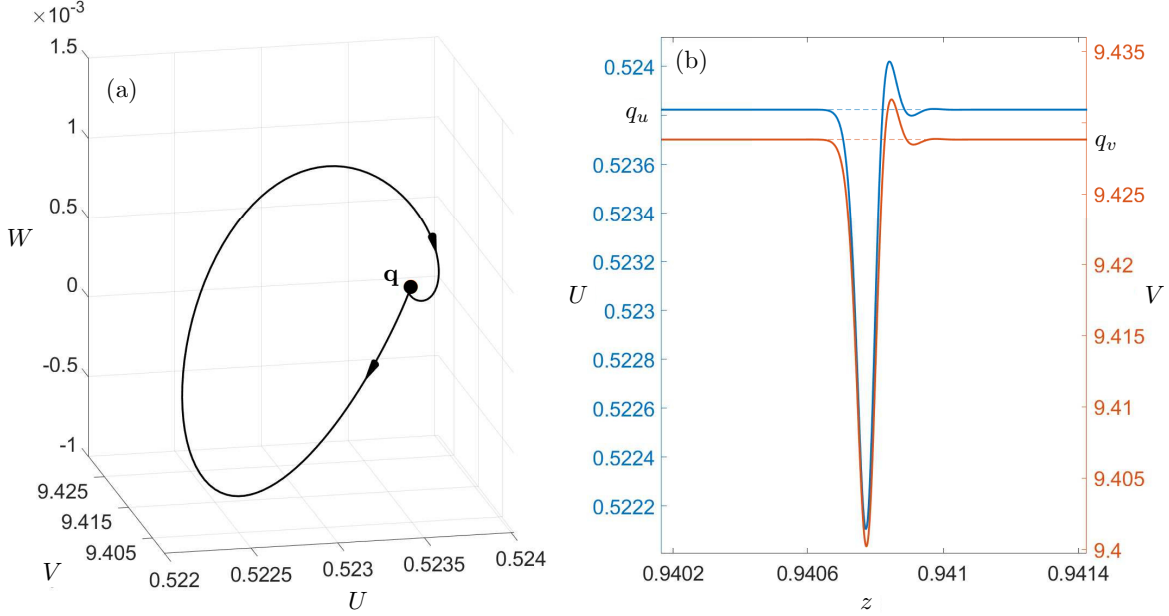


FIGURE 1. Profile of a wave pulse. Panel (a) shows a homoclinic orbit which joins the equilibrium \mathbf{q} to itself in the long term, projected onto the UVW space, while panel (b) shows the time series of U and V associated with this solution in blue and orange, respectively; here, the range of z values in the horizontal axis is restricted to the interval where the variables U and V develop the pulse. Parameter values are $a = 24$, $b = 19$, $g = 1$, $m = 0.0463358$ are taken from [5] while $c = 1$, $s = 100$, $d = 1.3080156$ are chosen after a bifurcation analysis in Figure 4.

Inspired by the biological origins of (2), we restrict our analysis of (4) to the set $\Omega = \{(U, V, W, R) \in \mathbb{R}^4 : U \geq 0, V \geq 0\}$. A traveling wave of (2) is any bounded solution of the system (4) contained in the domain Ω . These solutions are functions that “travel” in space, preserving their form as time goes by [23, 39, 38].

As we need to find bounded solutions of the system (4), we focus our attention on three special types of traveling waves: wave pulses, wave fronts, and wave trains [23]. Figure 1(a) shows an actual homoclinic orbit of (4) found with the method presented later, in Figure 5. The homoclinic orbit connects the equilibrium point $\mathbf{q} = (q_u, q_v, 0, 0)$ (given explicitly in Figure 3) to itself. The homoclinic connection is an orbit in the unstable manifold of \mathbf{q} , $W^u(\mathbf{q})$, that comes back to \mathbf{q} along its stable manifold $W^s(\mathbf{q})$, i.e., it is in the intersection $W^u(\mathbf{q}) \cap W^s(\mathbf{q})$. The time series of U and V associated with this connecting orbit are shown in Figure 1(b) in blue and orange, respectively. The profile of this solution is characterized by a large deviation (or pulse) in the amplitudes of U and V followed by a convergence back to the resting state. This corresponds to a wave pulse in the original system (2) that travels from a spatially homogeneous stationary solution to itself. Therefore, homoclinic orbits of (4) correspond to wave pulses of (2).

Figure 2(a) shows a heteroclinic orbit connecting \mathbf{q} to the equilibrium $\mathbf{p} = (p_u, p_v, 0, 0)$ (given explicitly below, in Figure 3). The heteroclinic connection is an orbit in $W^u(\mathbf{q})$ which moves away from \mathbf{q} , but it is also contained in the stable manifold of \mathbf{p} $W^s(\mathbf{p})$, and hence, heads toward \mathbf{p} . That is, this heteroclinic orbit lies in $W^u(\mathbf{q}) \cap W^s(\mathbf{p})$. This corresponds to a wave of (2) that makes the transition from one spatially homogeneous stationary solution to another as is shown in Figure 2(b).

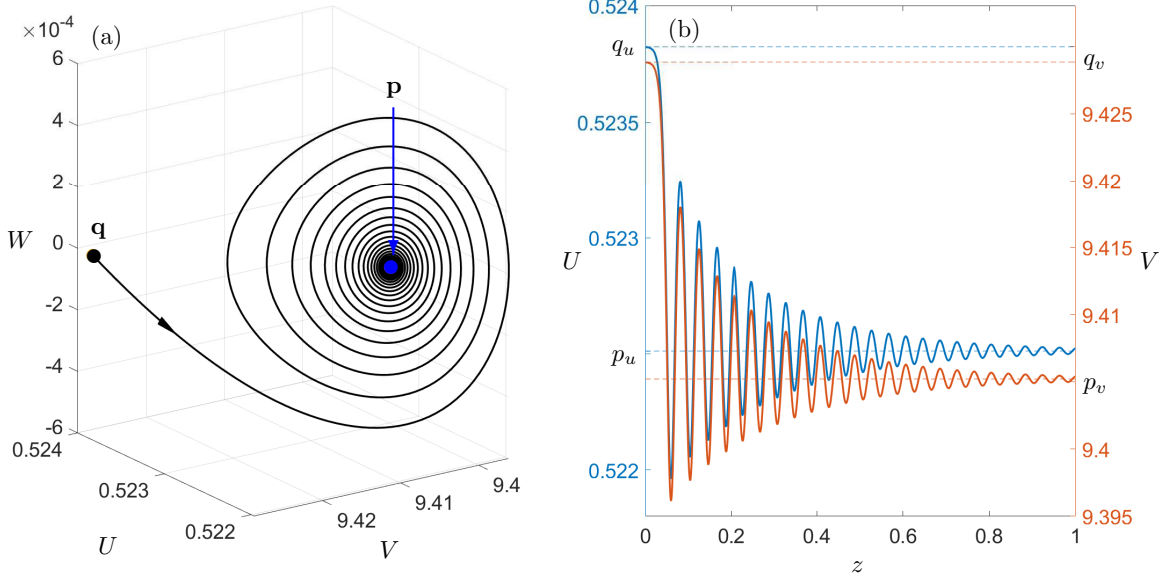


FIGURE 2. Profile of a wave front. Panel (a) shows a heteroclinic orbit from \mathbf{q} to \mathbf{p} , projected onto the UVW space, while panel (b) shows the time series of U and V associated with the same solution. Parameter values are the same as in Figure 1 except for $d = 2.2883206$, and $c = 0.4372925$.

The homoclinic and heteroclinic orbits (and their associated time series) as solutions of (4) are parameterized by $z \in (-\infty, \infty)$. However, for computational purposes, this independent variable is rescaled to $z \in [0, 1]$ in all our results; this is actually a standard procedure with numerical continuation methods (see [13, 28] and references therein). Moreover, in Figure 1 (and for every other wave pulse shown throughout this paper) we restrict the values of z to those compact subintervals of $]0, 1[$ where the pulses are easier to see.

The third kind of wave solution of (2) we are interested in is wave trains. These solutions correspond to periodic orbits of system (4), as is illustrated in Figure 3. For computational purposes, the period of every periodic orbit of (4) is rescaled to $T = 1$; see [13, 28]. In particular, in Figure 3 (and for every other wave train shown throughout this paper) we restrict the values of z to one such period of the cycle.

3. LOCAL STABILITY ANALYSIS

System (4) has at most five equilibrium points in Ω , which are given by $\mathbf{p}_0 = (0, 0, 0, 0)$, $\mathbf{p}_m = (m, 0, 0, 0)$, $\mathbf{p}_1 = (1, 0, 0, 0)$, $\mathbf{p} = (p_u, p_v, 0, 0)$, and $\mathbf{q} = (q_u, q_v, 0, 0)$, where

$$(5a) \quad q_u = \frac{bs(1+m) + \sqrt{bs\Delta}}{2bs}, \quad (5c) \quad p_u = \frac{bs(1+m) - \sqrt{bs\Delta}}{2bs},$$

$$(5b) \quad q_v = \frac{(b-g)}{g} q_u, \quad (5d) \quad p_v = \frac{(b-g)}{g} p_u,$$

provided that $\Delta = bs(m-1)^2 - 4a(b-g) \geq 0$, and $q_u, q_v, p_u, p_v \geq 0$. Under these conditions, we have the following result on the stability of \mathbf{p}_0 , \mathbf{p}_m and \mathbf{p}_1 :

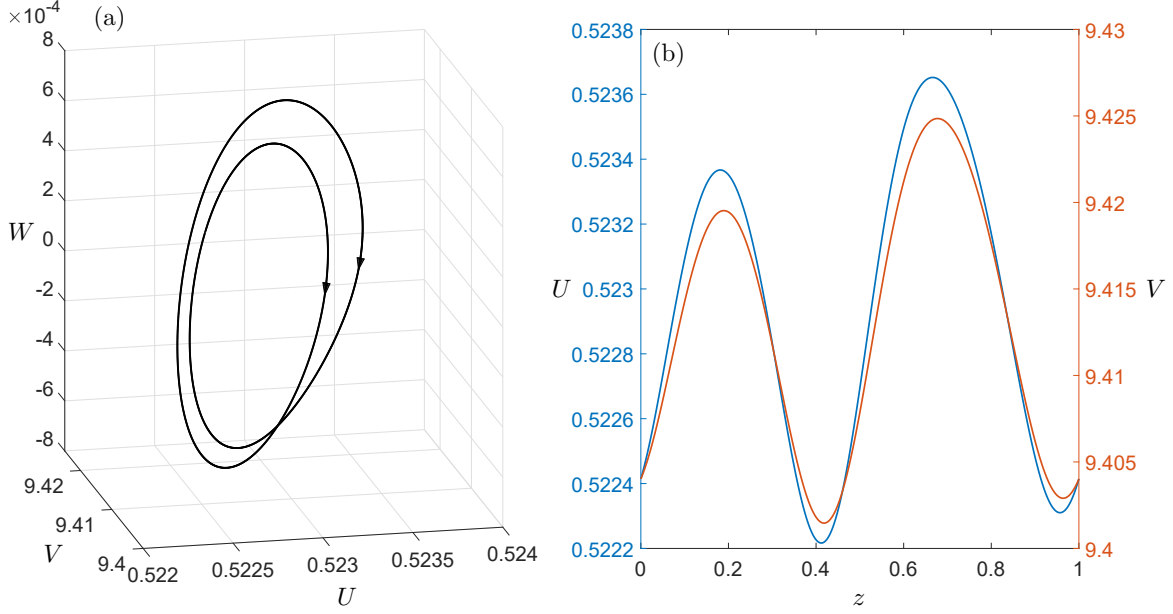


FIGURE 3. Profile of a wave train. Panel (a) shows a periodic orbit projected onto the UVW space, while panel (b) shows the time series of U and V contained in a (rescaled) period of length 1. Parameter values are the same as in Figure 1 except for $d = 1.3107$.

Proposition 1. *Let us consider the quantities*

$$\Delta_m^1 := c^2 + 4(g - b)m, \quad \Delta_m^2 := c^2 - 4d(1 - m)m^2s.$$

Then, system (4) satisfies the following statements:

- (1) \mathbf{p}_0 is an unstable non-hyperbolic equilibrium, $\dim(W^u(\mathbf{p}_0)) = 2$, and $\dim(W^c(\mathbf{p}_0)) = 2$.
- (2) If $b < g$, then \mathbf{p}_m and \mathbf{p}_1 are hyperbolic saddles, $\dim(W^s(\mathbf{p}_m)) = 1$, $\dim(W^u(\mathbf{p}_m)) = 3$, $\dim(W^s(\mathbf{p}_1)) = 2$, and $\dim(W^u(\mathbf{p}_1)) = 2$.
- (3) If $b > g$, then \mathbf{p}_m is a hyperbolic repeller, and \mathbf{p}_1 is a hyperbolic saddle, $\dim(W^s(\mathbf{p}_1)) = 1$, and $\dim(W^u(\mathbf{p}_1)) = 3$. In addition, if $\Delta_m^1 > 0$ and $\Delta_m^2 > 0$, then \mathbf{p}_m is a repelling node.

Proof. If we denote the vector field (4) by X , its Jacobian matrix evaluated at the points \mathbf{p}_0 , \mathbf{p}_m and \mathbf{p}_1 is given, respectively, by:

$$DX(\mathbf{p}_0) = \begin{pmatrix} 0 & 0 & 1 & 0 \\ 0 & 0 & 0 & 1 \\ 0 & 0 & \frac{c}{d} & 0 \\ 0 & 0 & 0 & c \end{pmatrix}, \quad DX(\mathbf{p}_m) = \begin{pmatrix} 0 & 0 & 1 & 0 \\ 0 & 0 & 0 & 1 \\ -\frac{(1-m)m^2s}{d} & \frac{am}{d} & \frac{c}{d} & 0 \\ 0 & (g-b)m & 0 & c \end{pmatrix},$$

$$\text{and } DX(\mathbf{p}_1) = \begin{pmatrix} 0 & 0 & 1 & 0 \\ 0 & 0 & 0 & 1 \\ \frac{(1-m)s}{d} & \frac{a}{d} & \frac{c}{d} & 0 \\ 0 & g-b & 0 & c \end{pmatrix}.$$

Denoting by λ_i^j the i -th eigenvalue of the equilibrium \mathbf{p}_j , $j \in \{0, 1, m\}$, then we see that

$$\begin{cases} \lambda_{1,2}^0 = 0, \\ \lambda_3^0 = \frac{c}{d} > 0, \\ \lambda_4^0 = c > 0. \end{cases} \quad \begin{cases} \lambda_{1,2}^m = \frac{c \pm \sqrt{\Delta_m^1}}{2}, \\ \lambda_{3,4}^m = \frac{c \pm \sqrt{\Delta_m^2}}{2d}, \end{cases} \quad \begin{cases} \lambda_{1,2}^1 = \frac{c \pm \sqrt{c^2 + 4(g-b)}}{2}, \\ \lambda_{3,4}^1 = \frac{c \pm \sqrt{c^2 + 4d(1-m)s}}{2d}. \end{cases}$$

Since $DX(\mathbf{p}_0)$ has two zero and two positive eigenvalues, then \mathbf{p}_0 is an unstable non-hyperbolic equilibrium. The remaining statements are direct consequences of the Hartman-Grobman theorem and the stable manifold theorem [21]. As for \mathbf{p}_m , since $0 < m < 1$, then $\Delta_m^2 = c^2 - 4d(1-m)m^2s < c^2$. Furthermore, if $b < g$, then $\Delta_m^1 = c^2 + 4(g-b)m > c^2$. Thus we have that

$$\lambda_1^m = \frac{c + \sqrt{\Delta_m^1}}{2} > 0, \quad \lambda_2^m = \frac{c - \sqrt{\Delta_m^1}}{2} < 0, \quad \text{Re}(\lambda_{3,4}^m) > 0,$$

which implies the desired result. On the other hand, if $b > g$, then $\Delta_m^1 < c^2$, which implies that $\lambda_2^m > 0$. In the particular case that $b > g$, $\Delta_m^1 > 0$ and $\Delta_m^2 > 0$, the eigenvalues $\lambda_{3,4}^m$ of $DX(\mathbf{p}_m)$ become real and positive and, hence, \mathbf{p}_m is a repelling node. Similarly, a sign analysis of the eigenvalues of $DX(\mathbf{p}_1)$ reveals the stability of \mathbf{p}_1 and the dimensions of its invariant manifolds. \square \square

Proposition 2. *If $b > g$ and $\Delta > 0$, then both equilibria \mathbf{p} and \mathbf{q} of (4) are in the domain Ω .*

Proof. It is immediate to see that if $\Delta > 0$, then \mathbf{p} and \mathbf{q} exist and are different. To see that $\mathbf{p}, \mathbf{q} \in \Omega$, note that if $b > g$ and $\Delta > 0$, then

$$\begin{aligned} bsm &> -a(b-g) \\ \Leftrightarrow 2bsm &> -4a(b-g) - 2bsm \\ \Leftrightarrow bs(m^2 + 2m + 1) &> -4a(b-g) + bs(m^2 - 2m + 1) \\ \Leftrightarrow b^2s^2(1+m)^2 &> bs\Delta \\ \Leftrightarrow bs(1+m) &> \sqrt{bs\Delta} \\ \Leftrightarrow q_u &> p_u > 0. \end{aligned}$$

Finally, since $q_v = (b-g)q_u/g$ and $p_v = (b-g)p_u/g$, the result follows. \square \square

To perform a stability analysis of the equilibria \mathbf{p} and \mathbf{q} by standard methods is a challenging task. Indeed, the Jacobian matrix of X evaluated at \mathbf{p} and \mathbf{q} are given, respectively, by

$$DX(\mathbf{p}) = \begin{pmatrix} 0 & 0 & 1 & 0 \\ 0 & 0 & 0 & 1 \\ a_{31} & a_{32} & \frac{c}{d} & 0 \\ a_{41} & a_{42} & 0 & c \end{pmatrix} \quad \text{and} \quad DX(\mathbf{q}) = \begin{pmatrix} 0 & 0 & 1 & 0 \\ 0 & 0 & 0 & 1 \\ b_{31} & b_{32} & \frac{c}{d} & 0 \\ b_{41} & b_{42} & 0 & c \end{pmatrix},$$

where

$$\begin{aligned} a_{31} &= \frac{2a(bg + g^2 - 2b^2) + b(b(m-1)^2s - (m+1)\sqrt{bs\Delta})}{2bdg} p_u, \\ b_{31} &= \frac{2a(bg + g^2 - 2b^2) + b(b(m-1)^2s + (m+1)\sqrt{bs\Delta})}{2bdg} q_u, \end{aligned}$$

and

$$\begin{aligned} a_{32} &= \frac{ag}{bd}p_u, & a_{41} &= -(b-g)p_v, & a_{42} &= (b-g)p_u. \\ b_{32} &= \frac{ag}{bd}q_u, & b_{41} &= -(b-g)q_v, & b_{42} &= (b-g)q_u. \end{aligned}$$

Hence, the computation of analytic expressions for the eigenvalues of $DX(\mathbf{p})$ and $DX(\mathbf{q})$ turns out to be a cumbersome goal. However, direct inspection of equilibrium coordinates reveals evidence of some local bifurcations. If $b = g$, then from (5) we have that $q_v = p_v = 0$, $q_u = 1$, and $p_u = m$, since

$$\frac{bs(1+m) \pm \sqrt{b^2s^2(m-1)^2}}{2bs} = \frac{1+m \pm (1-m)}{2}.$$

This implies that $\mathbf{q} = \mathbf{p}_1$ and $\mathbf{p} = \mathbf{p}_m$. Since, according to Lemma 1, there is a stability change for \mathbf{p}_1 and \mathbf{p}_m when $b = g$, this is an indication of a transcritical bifurcation. The equilibrium points \mathbf{q} and \mathbf{p}_1 collide and interchange their stability when $b = g$; a similar statement follows for \mathbf{p} and \mathbf{p}_m . On the other hand, if $\Delta = 0$, then $q_u = p_u$ and $q_v = p_v$, so that $\mathbf{q} = \mathbf{p}$. Since these two equilibria exist only if $\Delta > 0$, this is evidence of a saddle-node (or fold) bifurcation of equilibrium points. Formal proofs for these statements require the reduction of (4) into a one-parameter family of center manifolds on each case, followed by verification of certain genericity conditions; we refer to [21, 30] for more details. However, we opt to omit these proofs in favor of a focus on the analysis of global bifurcations in (4) and the emergence of traveling waves in (2).

4. BIFURCATION ANALYSIS

In this section, we present a bifurcation analysis of (4) performed with the standard continuation package AUTO. As a starting point, we consider parameters $a = 24$, $b = 19$, $g = 1$ and $s = 100$ fixed throughout this section and let d and m to vary. The fixed values of a, b, g and s correspond to those in [5] after the transformation (2). As in general the wave speed is a continuous function of the parameters system, i.e., $c = c(d, s, b, g, a, m)$, for the purpose of simplification we take the initial value $c = 1$ for the wave speed in (4). This approach can be thought of as an exploratory phase in which one navigates the possible preimages of $c(d, s, b, g, a, m) = 1$ in parameter space that allow solutions in the traveling frame of reference moving at speed $c = 1$. Later in Figure 9, we let c to vary in order to capture the existence and properties of the wave solutions by means of a wider range of preimage values of c .

The resulting bifurcation scenario in the (m, d) -plane is shown in Figure 4. Of special importance for us are the curves h_p and h_q which represent homoclinic bifurcations to \mathbf{p} and \mathbf{q} , respectively. We will address the technical details and consequences of these homoclinic bifurcations later in Figure 5. For the moment, it suffices to say that h_p is divided into two segments (labeled as h_p^c and h_p^s , respectively) by a codimension two Belyakov homoclinic point, labeled as B [6, 7]. The right-hand side endpoints of both h_p^c and h_q (marked with \times) correspond to the last points where we could obtain convergence of the computed solutions with AUTO.

Figure 4 also shows a curve of Hopf bifurcation at the equilibrium \mathbf{p} . This bifurcation curve is divided into two segments. The first one is a segment of supercritical Hopf bifurcation, labeled as H_p^- ; the other one is a segment of subcritical Hopf bifurcation, labeled as H_p^+ . The separation between both sides of the Hopf curve occurs at a codimension two Zero-Hopf bifurcation point (labeled as ZH) where the Hopf curve meets a Fold bifurcation curve F in a quadratic tangency. The curve labeled as PD corresponds to a period doubling bifurcation, while NS is a Neimark-Sacker (or torus) bifurcation curve. These two curves meet at a codimension two strong resonant point, R_2 . The horizontal dotted line in Figure 4 corresponds to $d = 1$ (or equivalently, $D_1 = D_2$ in (1)). While this line does not represent any bifurcation, it is useful to distinguish the phenomena encountered above it from that

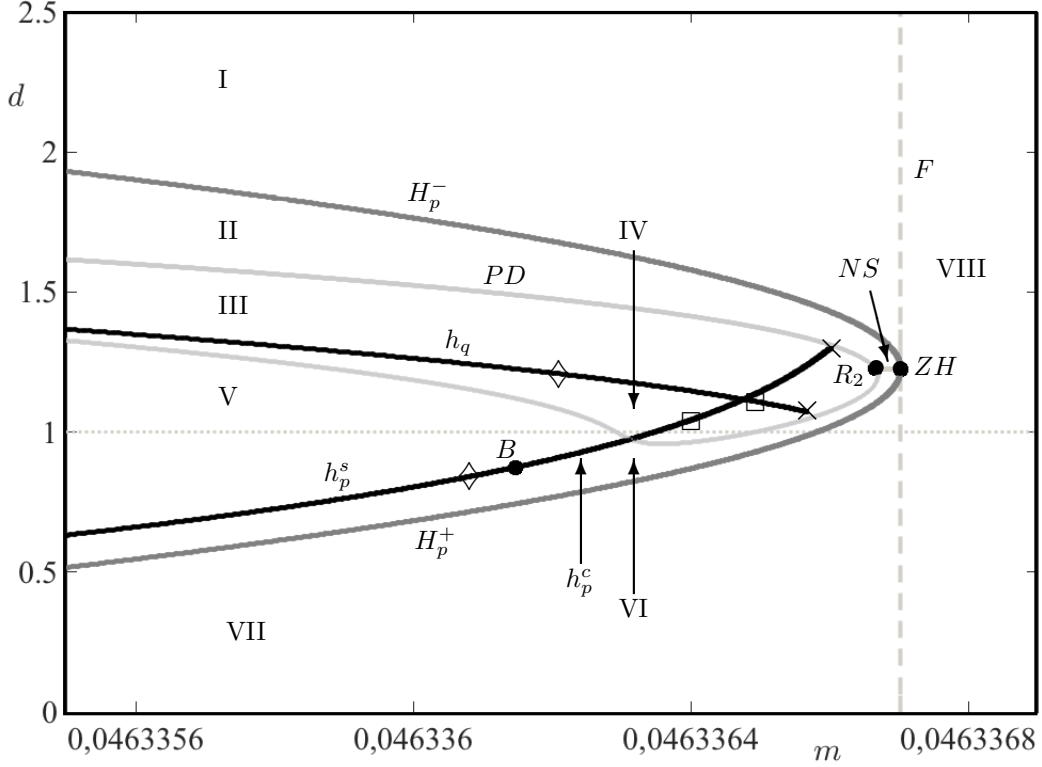


FIGURE 4. Bifurcation diagram of (4) in the (m, d) -plane space. Parameter values are the same as in Figure 1.

which occurs below it. Indeed, one must remember that if $d > 1$ (resp. $d < 1$), then \mathbf{u} has a higher (resp. lower) diffusion rate than \mathbf{v} .

The bifurcation curves in Figure 4 divide the (m, d) -plane into the open regions I-VIII. Region VIII is bounded to the left by the curve F , while I is delimited to its right by F , and below by H_p^- . Region II is surrounded by the curves H_p^- , NS , and PD ; while region III is enclosed by the curves PD , h_p^+ , and h_q . Furthermore, region IV is bounded by the segments h_q , h_p^+ , and PD , while region V is surrounded by the curves PD , h_p^- , and h_p^+ . Finally, region VI is enclosed by the curves h_p^- , h_p^+ , PD , NS , and H_p^+ , while region VII is delimited to the right by the curve F and above by H_p^+ .

It is relevant to note that the fold curve F corresponds to the equation $\Delta = 0$ in Figure 3. Hence, equilibrium points \mathbf{p} and \mathbf{q} exist on the left-hand side of the F curve (regions I-VII). In particular, if $(m, d) \in \text{I}$, both equilibria are hyperbolic. If (m, d) passes through the supercritical Hopf bifurcation curve H_p^- from region I towards region II, a limit cycle branches out from \mathbf{p} . While the Hopf bifurcation is supercritical, this criticality is restricted only to a suitable two-dimensional center manifold where the bifurcation takes place [21, 30]; the resulting periodic orbit in \mathbb{R}^4 is, in fact, of saddle type in region II. The stability properties of this cycle remain unchanged until this orbit undergoes a period doubling bifurcation when $(m, d) \in PD$. This periodic orbit faces a number of further bifurcations (not shown in Figure 4) as the point (m, d) moves towards the curve h_q where it gives rise to a homoclinic orbit.

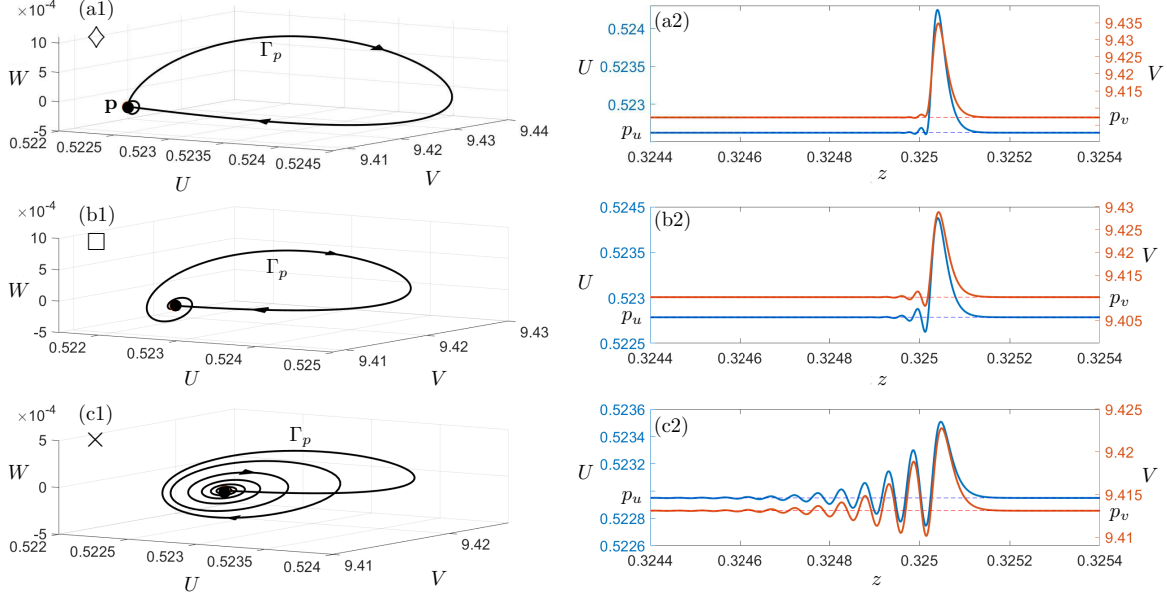


FIGURE 5. Homoclinic orbits to the equilibrium \mathbf{p} along the bifurcation curve h_p . Parameter values are $(m, d) = (0.0463361, 0.8740509)$ in panels (a1)-(a2), $(m, d) = (0.0463364, 1.0390163)$ in panels (b1)-(b2), and $(m, d) = (0.0463366, 1.2995479)$ in panels (c1)-(c2). The other parameters values are the same as in Figure 1.

We will address this transition again in Figure 6. On the other hand, when the point (m, d) crosses the NS curve from region II into region VI, an invariant torus bifurcates as a periodic orbit undergoes a Neimark-Sacker bifurcation.

Our bifurcation diagram in Figure 4 is just partially complete. Other codimension two strong resonances can be found along the NS bifurcation curve. Although the complete bifurcation diagram near these bifurcation points is yet to be known in its full complexity, one should expect the appearance of chaotic behavior when the point (m, d) is in a neighborhood of the NS curve; for further details, see [30]. Furthermore, bifurcation theory tells us that there is an infinite number of bifurcation curves in neighborhoods of both points B and R_2 . However, the full bifurcation picture near each of these points is not fully known from a theoretical point of view [30]. (We will address the complex dynamics that emerges due to the point B in Figure 5 below).

5. HOMOCLINIC BIFURCATIONS, WAVE PULSES, AND CHAOS

Figure 5 shows three different homoclinic orbits to the equilibrium \mathbf{p} in the left-hand side column, and their corresponding time series in the right-hand side column. The values of parameters (m, d) for each case correspond to those marked as \diamond , \square and \times along the curve h_p in Figure 4. In the left-hand side column of Figure 5, the homoclinic trajectories develop a rotational movement near \mathbf{p} before making a large excursion and returning to \mathbf{p} ; see the sequence of panels (a1)-(b1)-(c1). The amplitude of these oscillations increases as the point (m, d) moves to the right along the curve h_p . As a result, the corresponding wave pulses in panels (a2)-(b2)-(c2) feature an initial transient with increasingly larger oscillations —as (m, d) moves to the right along h_p — around the equilibrium values; in each case, this culminates in a large pulse before decaying back to the rest state. Indeed, the initial pattern of smaller amplitude oscillations of each wave takes most of a long interval of values of $z \in]0, 1[$ (i.e.,

it is a “slow” build-up in terms of z); while the large amplitude pulse occurs in a smaller interval (of order 10^{-4}) of parameter z (i.e. a “fast” discharge). Further, notice that both state variables \mathbf{u} and \mathbf{v} tend to increase and decrease simultaneously along any given traveling pulse.

The existence of the homoclinic orbit to \mathbf{p} implies the presence of chaotic dynamics in (4). Let us now state the main reasons for this claim. For any (m, d) in a neighbourhood of the curve h_p , the linearization of (4) at the equilibrium \mathbf{p} has one (stable) eigenvalue $\lambda^s < 0$ and three (unstable) eigenvalues $\lambda_{1,2}^u \in \mathbb{C}$, and $\lambda_3^u > 0$. In particular, $\lambda_{1,2}^u$ are complex conjugate with positive real part $\text{Re}(\lambda_{1,2}^u) > 0$. The equilibrium \mathbf{p} is called a *saddle-focus*. Figure 6 shows all the possible values of the eigenvalues of \mathbf{p} (in the complex plane) along the computed segment of the homoclinic bifurcation curve h_p . Namely, as parameters (m, d) are allowed to vary along the computed segment of the curve h_p in Figure 4, each eigenvalue of \mathbf{p} traces out a curve segment whose plots are shown in Figure 6. Among the unstable eigenvalues, the pair $\lambda_{1,2}^u$ are the closest to the imaginary axis $\text{Re}(\lambda) = 0$; hence, we say that $\lambda_{1,2}^u$ are the *leading unstable* eigenvalues. In this setting, if we define the so-called *saddle quantity* as $\sigma_1 = \lambda^s + \text{Re}(\lambda_{1,2}^u)$, Shilnikov’s theorems [21, 30, 48, 49] state that if $\sigma_1 > 0$, the homoclinic bifurcation is *simple* or *mild*. In this simple Shilnikov homoclinic bifurcation, a single (repelling) periodic orbit bifurcates from the homoclinic orbit on one side of the curve h_p . On the other hand, if $\sigma_1 < 0$, the homoclinic bifurcation is chaotic and gives rise to a wide range of complicated behavior in phase space. More specifically, one can find horseshoe dynamics in return maps defined in a neighbourhood of the homoclinic orbit. The suspension of the Smale horseshoes forms a hyperbolic invariant chaotic set which contains countably many periodic orbits of saddle-type. The horseshoe dynamics is robust under small parameter perturbations, i.e., the chaotic dynamics persist even when the homoclinic connection is broken; see [21, 30]. The segments labeled as h_p^s and h_p^c in Figure 4 correspond to simple and chaotic regimes, respectively, and are separated by the Belyakov point B where $\sigma_1 = 0$ [6, 7]. (Actually, at $(m, d) = B$, we have $\text{Re}(\lambda_{1,2}^u) = |\lambda^s| \approx 0.6654466$). Likewise, in Figure 6, the segments h_p^s and h_p^c along the curves for $\lambda_{1,2}^u$ correspond to $\sigma_1 > 0$ (simple) and $\sigma_1 < 0$ (chaotic), respectively, and are separated by the point labeled as B where $\sigma_1 = 0$. This same Belyakov transition is shown for the corresponding λ^s value as well (and is also labeled as B).

The bifurcation picture near the curve h_p in Figure 4 is just a partial representation of the full complexity one may encounter in this region of parameter space. Indeed, the saddle periodic orbits associated with the invariant chaotic set may also undergo further bifurcations such as period-doubling and torus bifurcations [21, 30]. Moreover, the presence of the chaotic h_p^c bifurcation and that of the Belyakov point B imply a very complicated structure (not shown) of infinitely many saddle-node and period-doubling bifurcations of periodic orbits as well as of subsidiary n -homoclinic orbits. Figure 7 shows a 2-homoclinic orbit to \mathbf{p} (in panel (a1)) and a 4-homoclinic orbit to \mathbf{p} (in panel (b1)), as well as their corresponding time series in panels (a2) and (b2), respectively. In general, n -homoclinic orbits are characterized by making $n - 1$ close passes near the equilibrium before closing up to form the connection; see panels (a1) and (b1). As a consequence, the corresponding traveling wave develops n pulses before setting down to the steady state values; see the 2-pulse and 4-pulse waves in panels (a1) and (b1), respectively. Moreover, for each of these subsidiary n -homoclinic orbits, the system exhibits horseshoe dynamics and chaos as in the original homoclinic scenario.

As for the homoclinic bifurcation h_q at the equilibrium \mathbf{q} , the associated Jacobian matrix of (4) at \mathbf{q} has a pair of complex-conjugate stable eigenvalues $\mu_{1,2}^s \in \mathbb{C}$ and a pair of complex-conjugate unstable eigenvalues $\mu_{1,2}^u \in \mathbb{C}$, with $\text{Re}(\mu_{1,2}^s) < 0$ and $\text{Re}(\mu_{1,2}^u) > 0$. The structure of the eigenvalues of \mathbf{q} as a function of $(m, d) \in h_q$ is shown in Figure 8. We say that \mathbf{q} is a *focus-focus* or *bi-focus*. The resulting homoclinic orbit Γ_q features a spiral-type convergence to \mathbf{q} as $z \rightarrow \pm\infty$. Figure 9 shows three different examples of such homoclinic orbit in the left column, and their respective time series in the right one. The values of parameters (m, d) for each case correspond to those marked as \diamond , \square and \times along the curve h_q in Figure 4. In the left-hand side column of Figure 9, the amplitude of

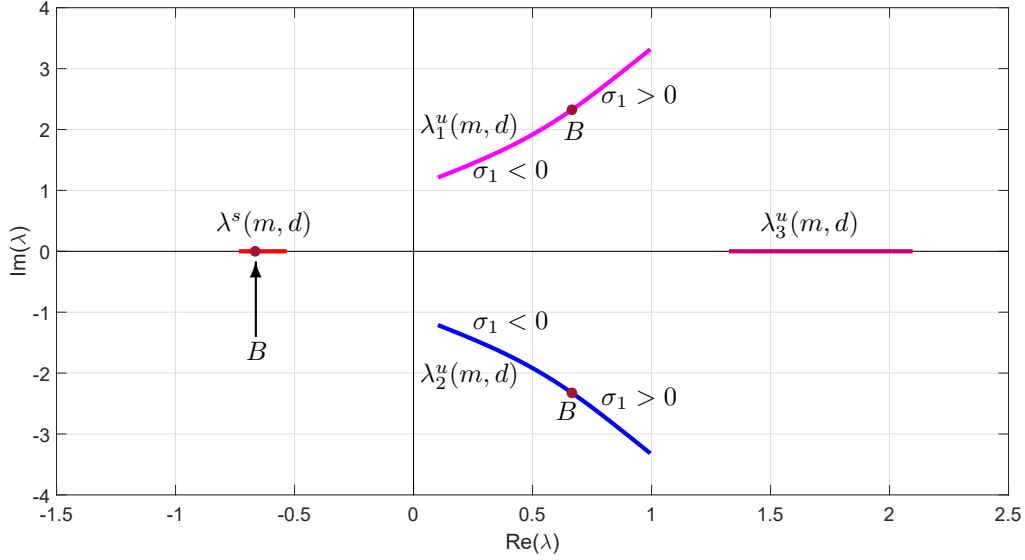


FIGURE 6. Eigenvalues of the Jacobian matrix $DX(\mathbf{p})$ continued for every (m, d) along the homoclinic bifurcation curve h_p in Figure 4.

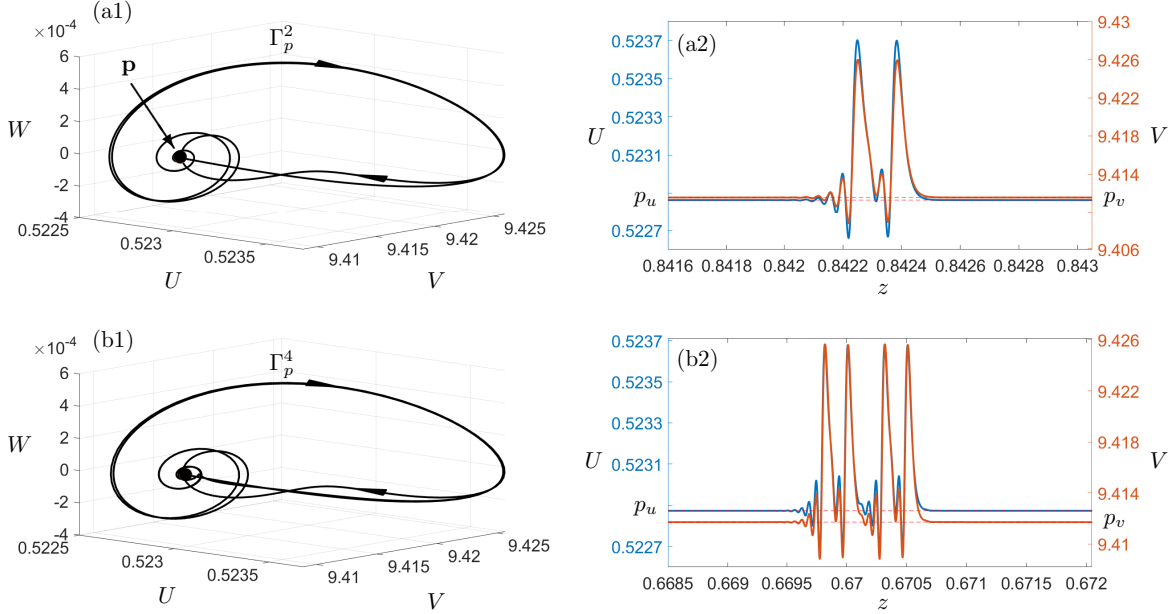


FIGURE 7. Panel (a1) shows Γ_p^2 , the 2-homoclinic orbit to \mathbf{p} , while panel (a2) shows its time series of U and V associated with Γ_p^2 . Similarly, panels (b1)-(b2) show a 2-homoclinic orbit and its associated 4-pulse wave, respectively. Parameter values are the same as in Figure 1 except for $(m, d) = (0.0463361, 1.1533894)$ in panels (a1)-(a2) and $(m, d) = (0.0463365, 1.1683875)$ in panels (b1)-(b2).

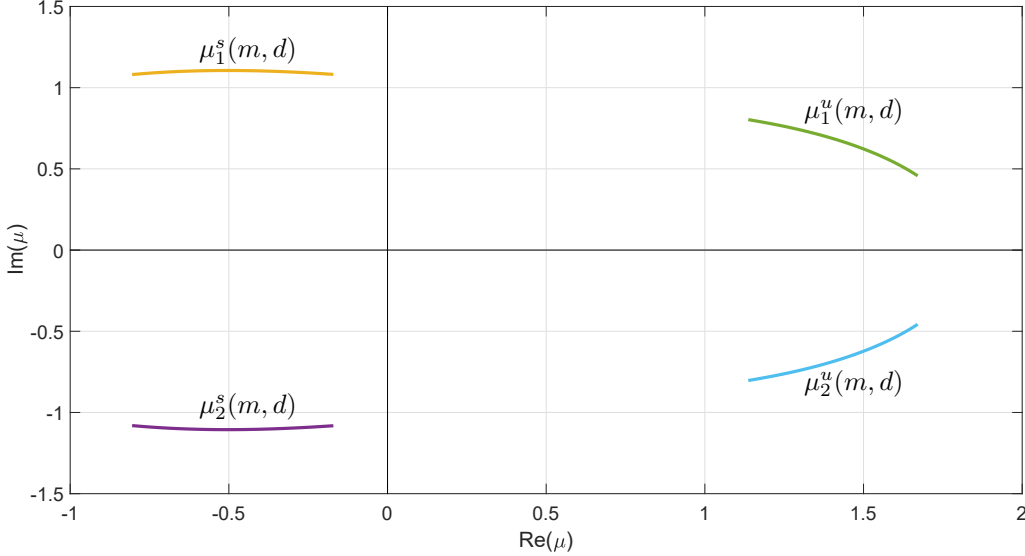


FIGURE 8. Eigenvalues $\mu_1^s(m, d)$, $\mu_2^s(m, d)$, $\mu_1^u(m, d)$ and $\mu_2^u(m, d)$ of $DX(\mathbf{q})$ continued for every (m, d) along the homoclinic bifurcation curve h_q in Figure 4.

the oscillations increases as the point (m, d) moves to the right along the curve h_q . As a result, the corresponding wave pulses in panels (a2)-(b2)-(c2) develop more oscillations —as (m, d) moves to the right along h_q — before converging to the equilibrium values as $z \rightarrow \infty$. The spirals and oscillations that are visible in panels (a1)-(b1)-(c1) and in panels (a2)-(b2)-(c2), respectively, are associated with the stable eigenvalues $\mu_{1,2}^s$ of \mathbf{q} . There is another set of oscillations as $z \rightarrow -\infty$ which are associated with the unstable eigenvalues $\mu_{1,2}^u$; however, since $\text{Im}(\mu_{1,2}^u) < \text{Im}(\mu_{1,2}^s)$ (see Figure 8 again), these spirals are relatively less pronounced and hard to see in Figure 9. Nevertheless, like the case of the homoclinic orbit to \mathbf{p} , here both \mathbf{u} and \mathbf{v} tend to increase and decrease simultaneously along any given traveling pulse.

The homoclinic bifurcation at the focus-focus equilibrium \mathbf{q} induces chaotic dynamics for every $(m, d) \in h_q$. Indeed, the presence of the homoclinic orbit Γ_q to a focus-focus equilibrium is accompanied by horseshoe dynamics in cross sections near Γ_q and, hence, an infinite number of saddle periodic orbits in a neighbourhood of Γ_q [30, 41]. Furthermore, in this setting, the *saddle quantity* is defined as $\sigma_2 = \text{Re}(\mu_{1,2}^s) + \text{Re}(\mu_{1,2}^u)$. Since $\sigma_2 > 0$ for every $(m, d) \in h_q$, it follows that there are no stable periodic orbits near Γ_q [19, 23].

In sum, any solution in a neighborhood of either Γ_p (in the chaotic case) or Γ_q tends to behave erratically and presents sensitive dependence to initial conditions. The corresponding orbit in the four-dimensional phase space of (4) spends a long transient visiting a strange hyperbolic invariant set before converging to an attractor. Hence, any bounded solution of (4) passing near either Γ_p (in the h_p^c side of the bifurcation) or Γ_q is associated with a chaotic traveling wave [41].

Figure 10(a) shows both homoclinic orbits Γ_p and Γ_q coexisting in phase space, while Figure 10(b1) and Figure 10(b2) show the time series of U and V associated with either trajectory. This special configuration occurs when the bifurcation curves h_p^c and h_q cross each other at $(m, d) \approx (0.046336476, 1.11668)$; see the bifurcation diagram of Figure 4. While this intersection point is not a new bifurcation, at these parameter values both classes of homoclinic orbits, Γ_q and Γ_p , coexist in phase space. Moreover, one

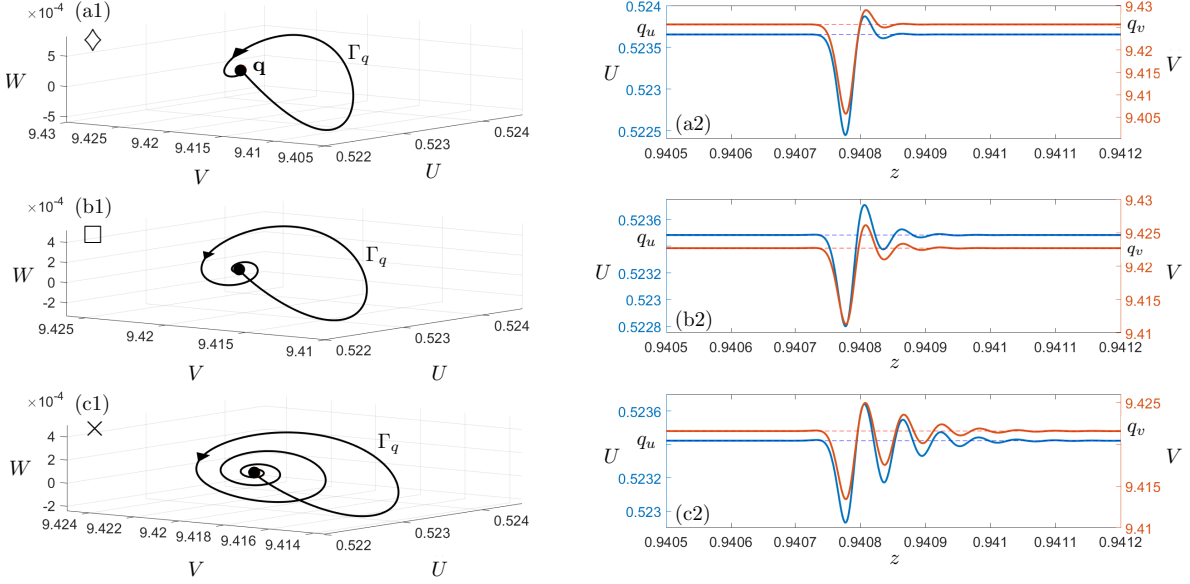


FIGURE 9. Homoclinic orbits to the equilibrium \mathbf{q} along the bifurcation curve h_q . Parameter values are $(m, d) = (0.0463362, 1.2091095)$ in panels (a1)-(a2), $(m, d) = (0.0463365, 1.1092036)$ in panels (b1)-(b2), and $(m, d) = (0.0463366, 1.0724625)$ in panels (c1)-(c2). The other parameters values are the same as in Figure 1.

obtains the coexistence of both chaotic invariant sets (each associated with one of the homoclinic trajectories) and, hence, the corresponding erratic behavior and sensitive dependence on initial conditions of nearby solutions.

6. PERIODIC ORBITS AND WAVE TRAINS

In this section we study the limit cycles existing in (4), their bifurcations, and their consequences for the nature of wave trains.

6.1. Period doubling phenomena. Let us consider the periodic orbit Γ which originates at the supercritical Hopf bifurcation H_p^- and track its successive bifurcations as parameter d is decreased and $m = 0.0463358$ remains fixed. When (m, d) crosses the PD curve from region II to III, the cycle Γ undergoes a period doubling bifurcation. As (m, d) enters region III, Γ changes its stability and a secondary limit cycle Γ^2 appears with approximately twice the period of Γ . As parameter d is further decreased, additional period doubling events occur (not shown in Figure 4). This is illustrated in Figure 11. Periodic orbits Γ^2 , Γ^4 and Γ^8 of periods 2, 4, and 8 times that of Γ , respectively, are shown in panels (a1)-(b1)-(c1). Panels (a2)-(b2)-(c2) show one period of the corresponding time series of U and V . Here, the actual periods of the solutions are rescaled to $T = 1$ for visualization and computational purposes [13]. As a consequence, as parameter d decreases and system (4) undergoes this sequence of period doubling bifurcations, the associated wave trains in panels (a2)-(b2)-(c2) display periodic patterns with doubling periods.

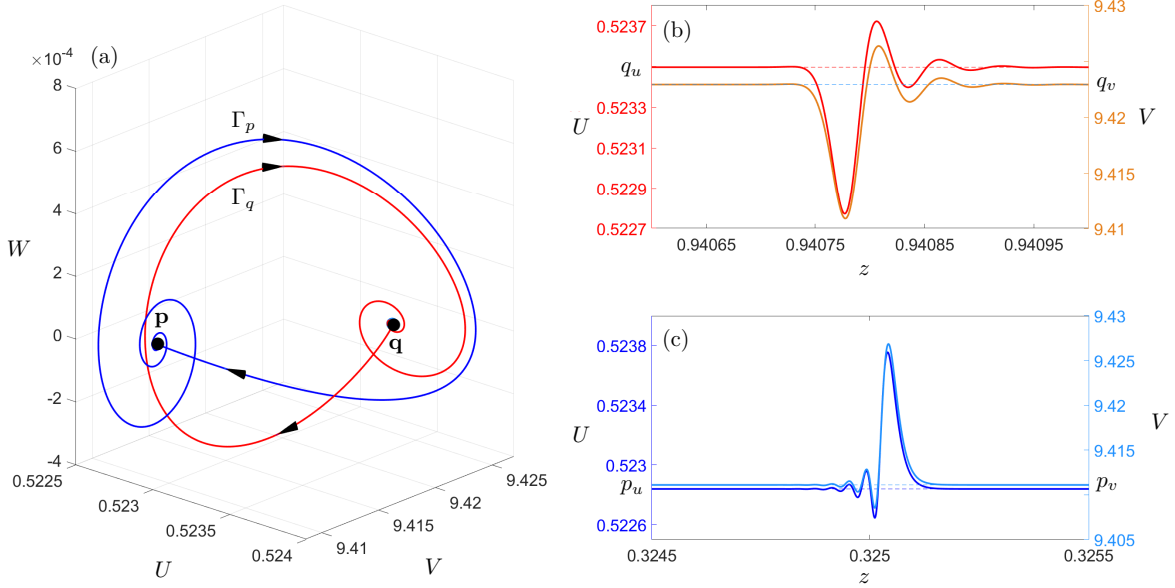


FIGURE 10. Panel (a) shows a projection of Γ_s and Γ_p onto the UVW space, when $(m, d) \approx (0.046336476, 1.11668) \in h_p^c \cap h_q$. Meanwhile, panel (b1) (resp. (b2)) shows the time series of U and V rendered in different color tones, associated with Γ_s (resp. Γ_p). The other parameter values are the same as in Figure 1.

6.2. Transition from wave trains to wave pulses. It is essential to highlight that when the point (m, d) crosses the PD curve from region II to region III, the cycle Γ does not disappear but just changes its stability. Figure 12 shows the graph of the period T of this cycle as a function of d . The bifurcation curve oscillates around the critical value $d^* \approx 1.3080156$ for which the homoclinic bifurcation h_q to \mathbf{q} occurs. The amplitude of the oscillations decreases rapidly as the homoclinic limit is approached when d tends to d^* ; see [30] and references therein. Indeed, the “snaking” behavior of the bifurcation curve is typical of the main branch of periodic orbits near chaotic saddle-focus and focus-focus homoclinic bifurcations [19, 52]. At each of the infinitely many folds of the curve, a pair of periodic orbits is created via a saddle-node bifurcation of limit cycles. Some of the periodic orbits in this branch may further undergo period-doubling bifurcations changing their stability along the bifurcation curve. Figure 13 shows three such periodic orbits, labelled as Γ_A , Γ_B , and Γ_C , respectively, corresponding to the points A , B and C in Figure 12. As d approaches d^* , the cycles pass increasingly closer to \mathbf{q} (see the sequence of panels (a1)-(b1)-(c1) in Figure 13). As a result, one obtains wave trains which spend longer transients close to the equilibrium values (see the sequence of panels (a2)-(b2)-(c2) in which the period T of each cycle is rescaled to 1). Hence, one can think of the homoclinic orbit Γ_q (and its corresponding wave pulse) as the limit of this sequence of periodic orbits (resp. wave trains) of increasing period as $d \rightarrow d^*$. Furthermore, each of the periodic orbits bifurcated from the period doubling phenomena in subsection 6.1 may also increase their periods and undergo a convergence to n -homoclinic orbits in a similar fashion. Some of these secondary homoclinic bifurcations are mentioned before in Figure 5 and shown in Figure 7.

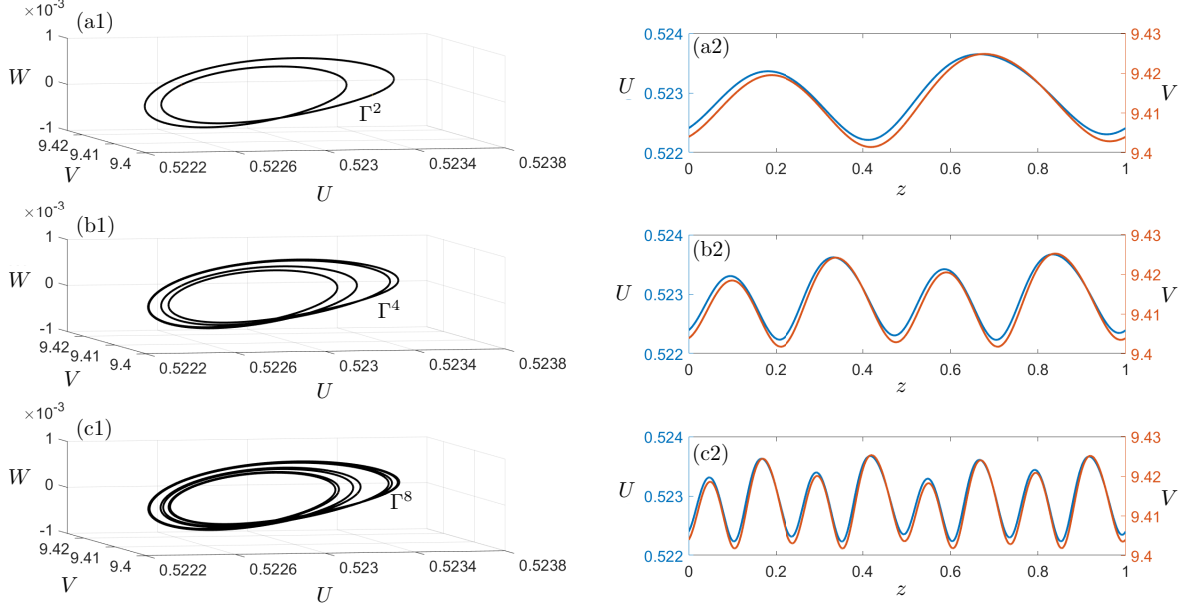


FIGURE 11. The different periodic orbits (panels (a1), (b1) and (c1)) and associated wave trains (panels (a2), (b2) and (c2)) emerging from successive period doubling bifurcations. While the periods in the time series are uniformly rescaled to 1 for computational purposes, the actual periods of the cycles are $T = 12.1829$ for Γ^2 , $T = 24.3659$ for Γ^4 , and $T = 48.7318$ for Γ^8 . Parameter values are $d = 1.469369$ (in panels (a)), $d = 1.4607309$ (in panels (b)), and $d = 1.4590971$ (in panels (c)), with $m = 0.0463362$ fixed. The other parameters as are as in Figure 1.

7. HETEROCLINIC CONNECTIONS AND WAVE FRONTS

Figure 14(a) shows a heteroclinic orbit, labeled as $\Gamma_{q,p}$, obtained for $(m, d) = (0.0463358, 2.4)$ in region I. The heteroclinic connection is oriented from \mathbf{q} to \mathbf{p} as parameter z —that which parametrizes the curve—is increased. The resulting time series are shown in Figure 14(b), and they correspond to a wave front traveling from the steady state \mathbf{q} that decays exponentially to \mathbf{p} in synchronized oscillatory fashion. This non-monotonic behavior is explained by the presence of a pair of stable complex-conjugate eigenvalues (with negative real part) of \mathbf{p} when parameters (m, d) are in region I. The connecting orbit $\Gamma_{q,p}$ lies in the intersection of the global invariant manifolds $W^s(\mathbf{p})$ and $W^u(\mathbf{q})$. Namely, $\Gamma_{q,p}$ is contained in the two-dimensional unstable manifold $W^u(\mathbf{q})$ —represented in Figure 14(a) as a transparent red surface—and approaches \mathbf{p} along its three-dimensional stable manifold $W^s(\mathbf{p})$ (not shown). Moreover, since $W^s(\mathbf{p})$ and $W^u(\mathbf{q})$ are, respectively, three and two-dimensional immersed smooth manifolds in \mathbb{R}^4 , it follows that the intersection $W^s(\mathbf{p}) \cap W^u(\mathbf{q})$ is transverse [22]. As a consequence, the heteroclinic orbit $\Gamma_{q,p}$ and, hence, its associated wave front persist under small parameter variations. Under small changes to the parameter values in region I, the resulting wave front may vary the amplitude of its oscillations and the actual asymptotic values, but the qualitative behavior of the traveling front remains unaltered throughout.

As parameter (m, d) crosses the H_p^- curve from region I to region II, a pair of stable eigenvalues of \mathbf{p} cross the imaginary axis and become unstable; in the process, a limit cycle branches from \mathbf{p}

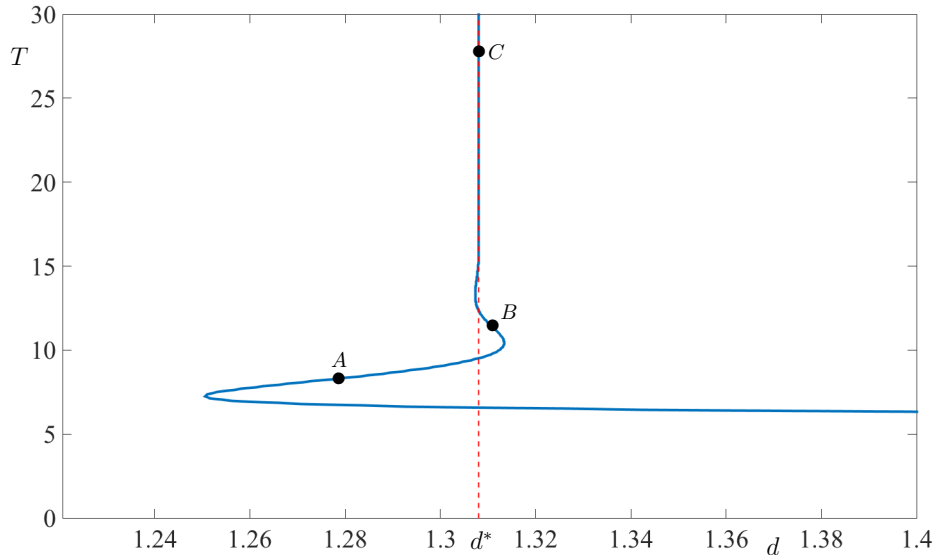


FIGURE 12. Bifurcation curve of the period T of periodic orbits with respect to d , near the homoclinic bifurcation at \mathbf{p} . Here $m = 0.0463358$ is fixed and the other parameters as are as in Figure 1.

in a supercritical Hopf bifurcation. Hence, in region II, $W^s(\mathbf{p})$ is a one-dimensional manifold and the connection $\Gamma_{q,p}$ does not exist. Rather, it is replaced by a heteroclinic orbit that joins \mathbf{q} to the bifurcated cycle. Figure 15(a) shows the bifurcated periodic orbit, labeled as γ after (m, d) has entered region II from region I. The unstable manifold $W^u(\mathbf{q})$ (red surface) rolls up around γ and intersects the three-dimensional stable manifold $W^s(\gamma)$ (not shown) transversally along a heteroclinic orbit, labeled as $\Gamma_{q,\gamma}$. This heteroclinic connection is associated with the traveling wave shown in Figure 15(b); this is a front transitioning from the steady state at \mathbf{q} into a periodic pattern around \mathbf{p} . The heteroclinic orbit $\Gamma_{q,\gamma}$ (and its traveling front) is preserved in an open subset of region II, and it disappears when (m, d) crosses the PD curve towards region III as γ loses its stability in a period doubling bifurcation.

If (m, d) is in an open subset of regions III, IV, and V, one can find a wave front traveling from \mathbf{p} to \mathbf{q} . This front travels in the opposite direction to that in Figure 14 and, hence, it corresponds to a third kind of wave. The wave front traveling from \mathbf{p} to \mathbf{q} is shown in Figure 16(b). The wave begins at the steady state \mathbf{p} with oscillations of increasing amplitude until it settles at \mathbf{q} . This front corresponds to an intersection of the manifolds $W^s(\mathbf{q})$ and $W^u(\mathbf{p})$ forming a heteroclinic orbit in the phase space of (4); Figure 16(a) shows the heteroclinic orbit (labelled as $\Gamma_{p,q}$) and the two-dimensional manifold $W^s(\mathbf{q})$ of \mathbf{q} as a transparent blue surface. The connection $\Gamma_{p,q}$ is an orbit in the three dimensional unstable manifold $W^u(\mathbf{p})$ which lies on $W^s(\mathbf{q})$ to converge to \mathbf{q} .

8. MULTIPLE WAVE FRONTS AT THE FOCUS-FOCUS HOMOCLINIC BIFURCATION

In Figure 5, we described the complicated dynamics that can be found near the focus-focus homoclinic bifurcation Γ_q when $(m, d) \in h_q$. One of the consequences of this fact is the appearance of multiple wave fronts of type $\Gamma_{p,q}$ (described in Figure 7) which coexist with the main wave pulse Γ_q . We explain this finding here by direct, close inspection of the invariant manifolds involved.

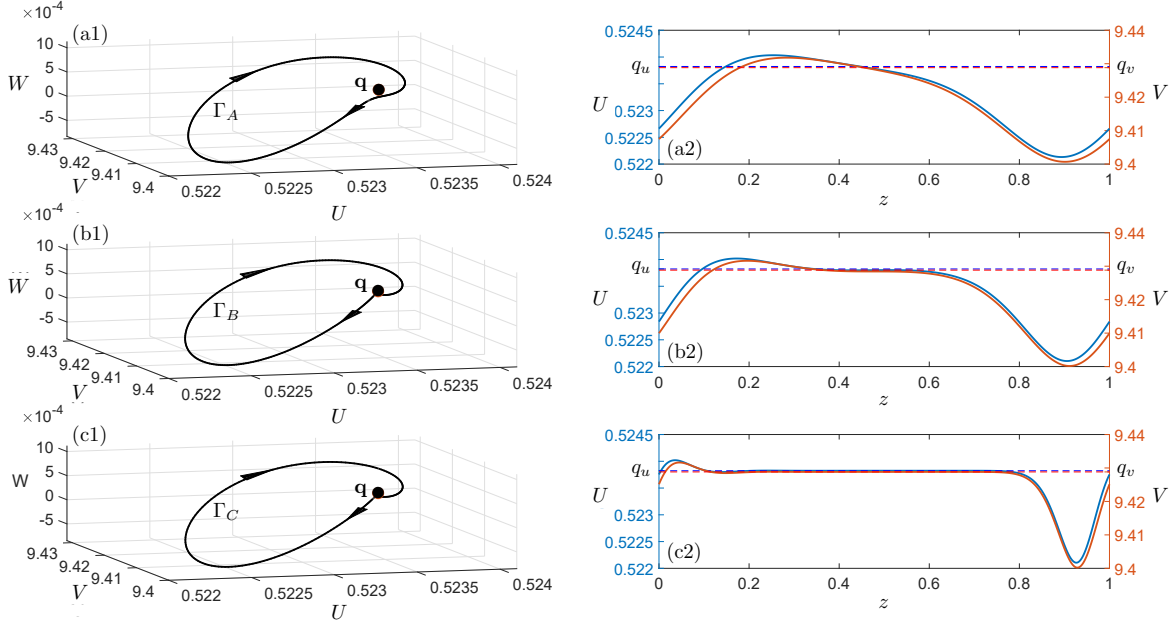


FIGURE 13. The different periodic orbits Γ_A , Γ_B and Γ_C (in panels (a1), (b1) and (c1)) and associated wave trains (panels (a2), (b2) and (c2)). While the periods in the time series are uniformly rescaled to 1 for computational purposes, the actual periods of the cycles are $T = 8.2967$ for Γ_A , $T = 11.4382$ for Γ_B , and $T = 27.8801$ for Γ_C . Parameter values are $d = 1.2785$ (in panels (a)), $d = 1.3107$ (in panels (b)), and $d = 1.3080$ (in panels (c)), with $m = 0.0463358$ fixed. The other parameters as are as in Figure 1.

Figure 17 shows the projection of $W^s(\mathbf{q})$ onto the UVW space, when

$$(m, d) \approx (0.0463358, 1.3080156) \in h_q.$$

Also shown is the homoclinic orbit Γ_q (red curve). The two-dimensional manifold $W^s(\mathbf{q})$ is rendered as a transparent blue surface. Some orbits in $W^s(\mathbf{q})$ lie in the three-dimensional unstable manifold $W^u(\mathbf{p})$ forming heteroclinic connections. In our computations, we detected seven heteroclinic orbits contained in $W^u(\mathbf{p}) \cap W^s(\mathbf{q})$. Most of these heteroclinic connections are very close to one another and very hard to distinguish from each other; we show one of them (cyan curve labeled as $\Gamma_{p,q}$) in Figure 17. Each of these seven heteroclinic orbits corresponds to a different wave front traveling from \mathbf{p} to \mathbf{q} , which are present in the system at the same time.

Further, there are also 2- and 3-homoclinic orbits to \mathbf{q} in $W^u(\mathbf{q}) \cap W^s(\mathbf{q})$, coexisting with the primary homoclinic orbit and the heteroclinic connections in phase space; we opted to not show these subsidiary homoclinic orbits in Figure 17 for visualization purposes. Figure 18(a) shows the profiles of U associated with the primary wave pulse Γ_q and the secondary 2- and 3-pulse waves (labeled as Γ_q^2 and Γ_q^3 , respectively) associated with the secondary homoclinic orbits. In turn, Figure 18(b) shows three representative traveling fronts associated with the family of heteroclinic orbits in phase space. The existence of these families of wave fronts when $(m, d) \in h_q$ indicates that there must be a sequence of associated global bifurcations as (m, d) approaches the h_q curve. At each of these bifurcation events, the manifolds $W^u(\mathbf{p})$ and $W^s(\mathbf{q})$ intersect tangentially in \mathbb{R}^4 along a (newly created) heteroclinic orbit. As (m, d) moves closer to the h_q curve, the intersection becomes transversal and the heteroclinic

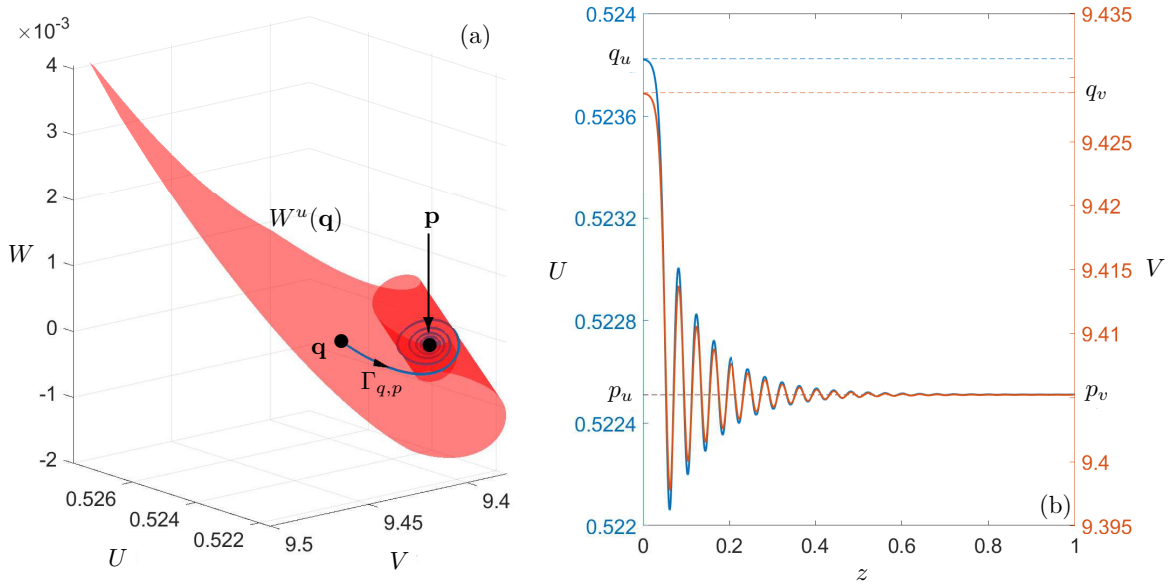


FIGURE 14. The connecting orbit $\Gamma_{q,p}$ lies in the intersection of the global invariant manifolds $W^s(\mathbf{p})$ and $W^u(\mathbf{q})$ in panel (a). In panel (b) the associated wave front travels from the steady state \mathbf{q} and its amplitude decays exponentially fast to \mathbf{p} showing oscillations. Parameter values are $(m, d) = (0.0463358, 2.4)$ and the other parameters remain fixed as in Figure 1.

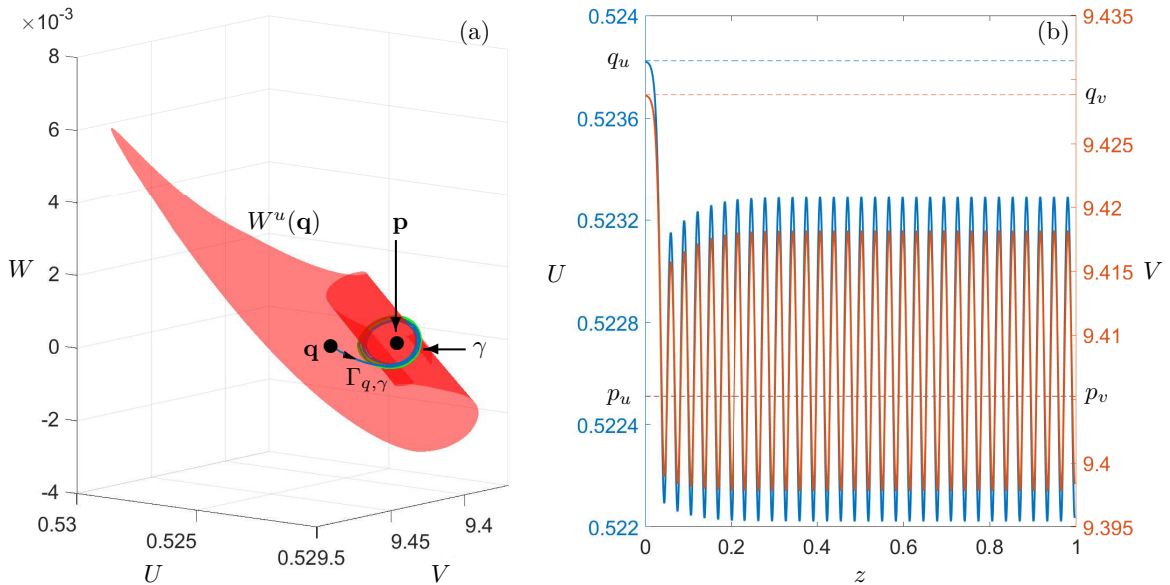


FIGURE 15. The connecting orbit $\Gamma_{q,\gamma}$ lies in the intersection of the global invariant manifolds $W^s(\gamma)$ and $W^u(\mathbf{q})$ in panel (a). The associated wave front travels from the steady state \mathbf{q} and adopts a periodic behavior oscillating around the equilibrium values of \mathbf{p} in panel (b). Parameter values are $(m, d) = (0.0463358, 1.7)$ and the other parameters remain fixed as in Figure 1.

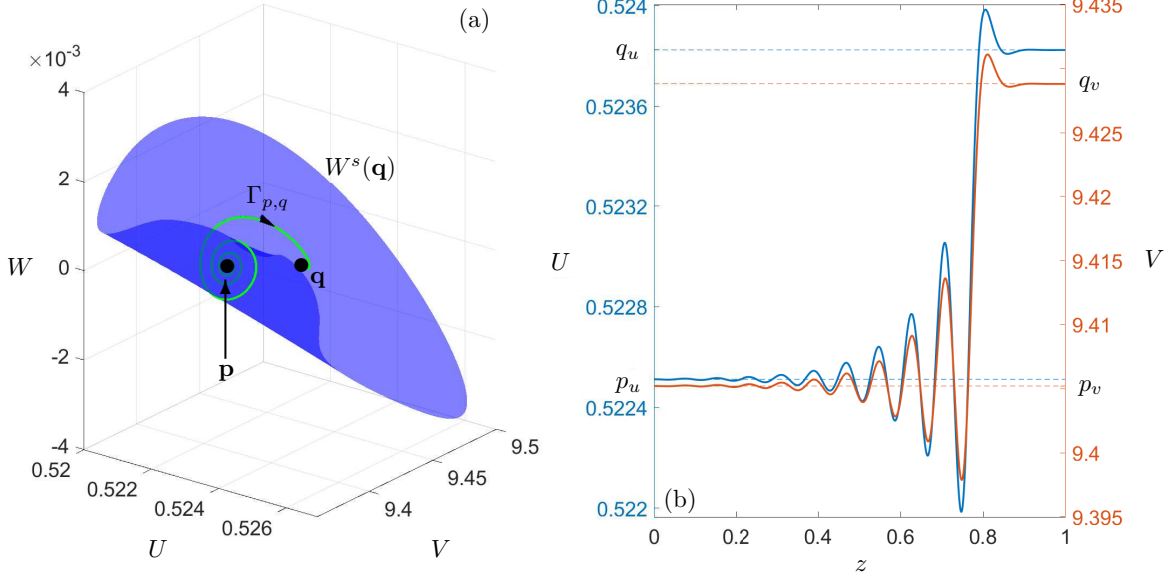


FIGURE 16. The connecting orbit $\Gamma_{p,q}$ lies in the intersection of the global invariant manifolds $W^u(\mathbf{p})$ and $W^s(\mathbf{q})$ in panel (a). In panel (b) the associated wave front travels from the steady state \mathbf{p} and its amplitude increases exponentially fast before settling down at \mathbf{q} . Parameter values are $(m, d) = (0.0463358, 1.4)$ and the other parameters remain fixed as in Figure 1.

orbit persists under small parameter variations. Similar events happen in the case of the secondary homoclinic orbits in the intersection of $W^u(\mathbf{q})$ and $W^s(\mathbf{q})$, that explain the emergence of 2- and 3-pulse waves as parameters (m, d) approach the h_q curve.

The method to detect these connections is explained as follows. If $W^s(\mathbf{q})$ contains a heteroclinic orbit flowing from \mathbf{p} to \mathbf{q} , such trajectory is approximated by a bounded solution contained in a family $\widehat{W}_{\delta, T}^s(\mathbf{q})$ of orbit segments passing sufficiently close to \mathbf{p} and satisfying a two-point boundary value problem. Every solution in $\widehat{W}_{\delta, T}^s(\mathbf{q})$ is continued up to an integration time T (which is a free parameter in this continuation) and is parametrized by a unique location $\delta \in [0, 1)$ in a fundamental domain; see [4, 6, 28] for more details. Indeed, if a heteroclinic orbit exists, the two-parameter continuation procedure effectively stops as the integration time diverges. In practice, an approximation of such connecting orbit is obtained at some specific $\delta = \delta^* \in [0, 1)$ with a large integration time $T = -T^*$. A similar criterium can be used to detect secondary n -homoclinic orbits to \mathbf{q} as orbit segments ending near \mathbf{q} as the integration time T diverges. For instance, in Figure ??, the fundamental domain $\delta \in [0, 1)$ is divided into 13 sub-segments by the values $0 < \delta_1 < \delta_2 < \dots < \delta_{12} < 1$. The heteroclinic connections correspond to $\delta_1 \approx 0.317181$, $\delta_2 \approx 0.317265$, $\delta_6 \approx 0.319579$, $\delta_8 \approx 0.319621$, $\delta_9 \approx 0.319904$, $\delta_{11} \approx 0.319917$ and $\delta_{12} \approx 0.331911$. On the other hand, we have the primary homoclinic orbit at $\delta_7 \approx 0.319616$, and four secondary homoclinic orbits at $\delta_3 \approx 0.317284$, $\delta_4 \approx 0.317285$, $\delta_5 \approx 0.317285$ and $\delta_{10} \approx 0.319906$.

9. THE INFLUENCE OF PROPAGATION SPEED AND DIFFUSION RATIO

The study and results reported so far in sections 4–8 were produced with fixed wave speed $c = 1$. Here we ask ourselves if there is a minimum wave speed needed for the existence of some of the traveling waves we have found. To this end, we consider the homoclinic orbits Γ_p and Γ_q existing at

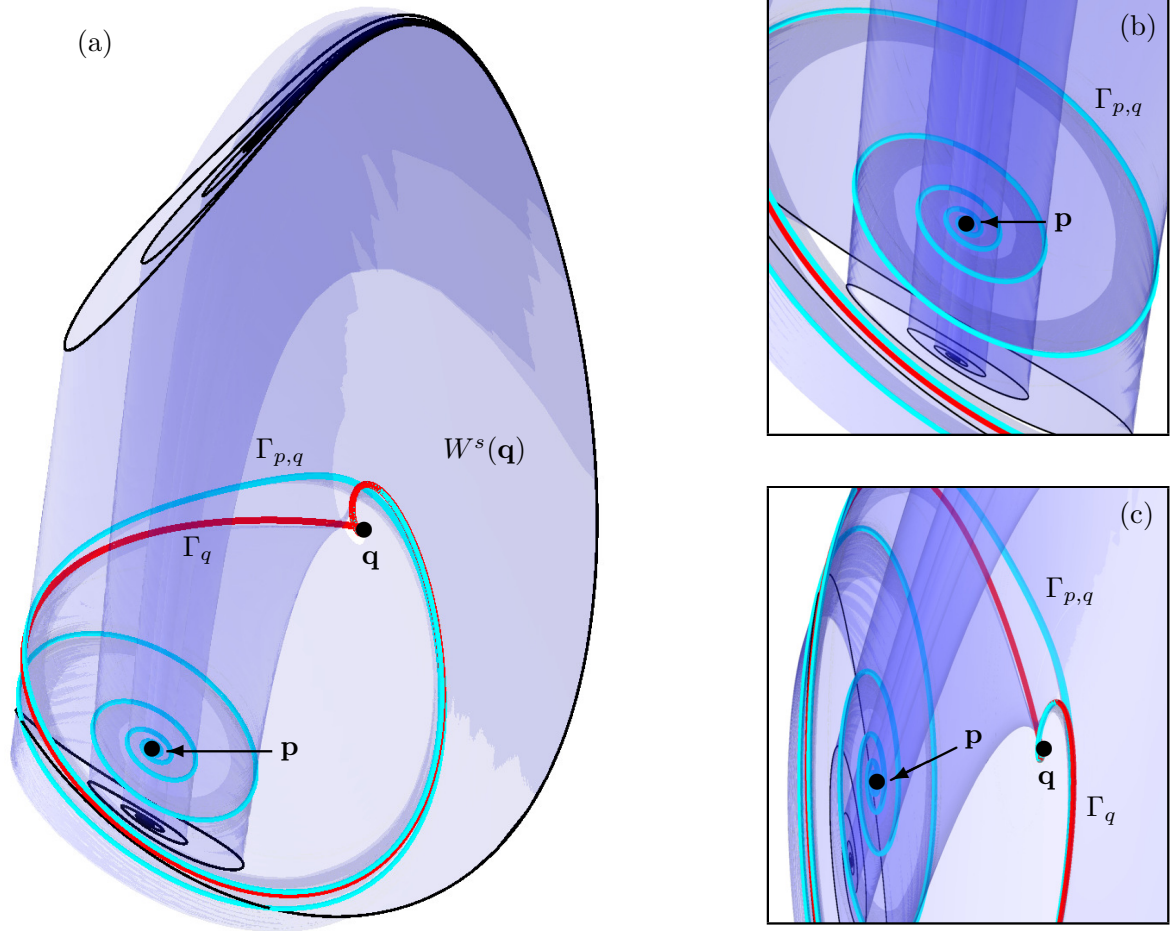


FIGURE 17. The stable manifold $W^s(\mathbf{q})$ of \mathbf{q} projected onto the UVW space in panel (a) when $(m, d) \approx (0.0463358, 1.3080156) \in h_q$. The manifold $W^s(\mathbf{q})$ contains a family of coexisting heteroclinic orbits which join the equilibrium \mathbf{p} to \mathbf{q} as well as the primary focus-focus homoclinic connection Γ_q to \mathbf{q} . One of such heteroclinic orbits is represented by the trajectory $\Gamma_{p,q}$. Panels (b) and (c) show enlargements near the equilibria \mathbf{p} and \mathbf{q} , respectively. The other parameter values are the same as in Figure 1.

the curves h_p and h_q , respectively, when $m \approx 0.0463358$, and continue them in parameters c and d . Figure 19 shows the homoclinic bifurcation curves h_p and h_q in the (c, d) -plane. The existence of both homoclinic orbits is determined by a positive correlation between the wave speed c and the diffusion ratio d ; namely, as c decreases, the wave pulses exist provided d becomes sufficiently small.

In the case of h_p , the relation between c and d in Figure 19 is almost linear for $c \geq 0.1$. Indeed the curve h_p can be approximated as $d \approx 0.2925828c + 0.4333269$, for $0.1 \leq c < 1$, with a root mean square error $e = 0.00521$. In particular, the computed segment of the curve h_p is located in the halfspace $d < 1$. Hence, this kind of pulse wave with small wave speed $c < 1$ occurs only if V propagates in a more efficient way than U . On the other hand, as c decreases below 0.01, the

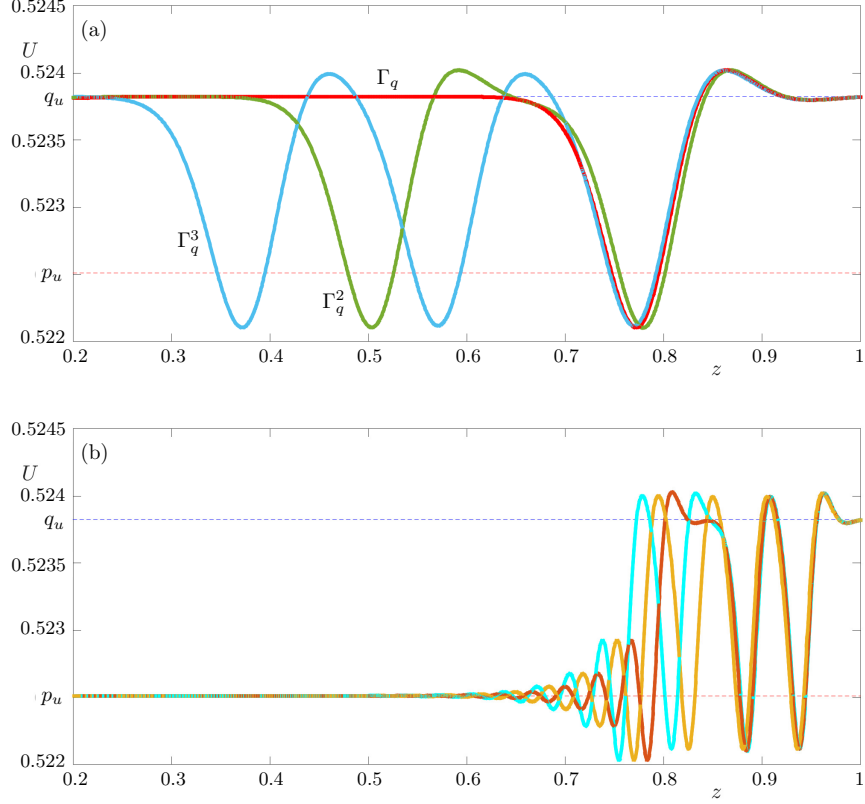


FIGURE 18. Profiles of U associated with the wave pulses Γ_q , Γ_q^2 and Γ_q^3 in panel (a); and three representative traveling fronts $\Gamma_{p,q}^1$, $\Gamma_{p,q}^2$, and $\Gamma_{p,q}^3$ in panel (b), when $(m, d) \approx (0.0463358, 1.3080156) \in h_q$. The other parameter values are the same as in Figure 1.

diffusion ratio d drops abruptly in a non linear way in the form $d = \mathcal{O}(c^{1/2})$; see Figure 19(c). As c is further decreased, the continuation procedure loses precision and the last point where we get convergence of the numerical scheme is at $c_{\min} = 0.0016767$. Figure 20 shows the homoclinic orbit Γ_p when $(c, d) = (0.0479321, 0.4449391)$ in panel (a), and its corresponding time series in panel (b). In panel (a), the orbit Γ_p performs many low-amplitude turns in $W_{\text{loc}}^u(\mathbf{p})$ before developing the long excursion. The corresponding wave in panel (b) shows a slow pattern (in terms of z) of small amplitude oscillations followed by a fast large amplitude pulse in a small interval (of order 10^{-4}) of parameter z , similar to typical dynamic behaviors with different time scales. Indeed, if the relation $d = \mathcal{O}(c^{1/2})$ still holds for $c \rightarrow 0$, then both (3) and (4) become singular as $c \rightarrow 0$ and $d \rightarrow 0$; while these systems in the singular limit may be studied with tools from geometric singular perturbation theory [18], this is beyond the scope of this work. Nevertheless, solutions $u(x, t) = U(x + ct)$, $v(x, t) = V(x + ct)$ of (2) as $c \rightarrow 0$ and $d = D_1/D_2 \rightarrow 0$ correspond to stationary waves in which, effectively, only the propagation of V is observable in the length scale x .

As for the bifurcation curve h_q in Figure 19(a)-(b), the dependence between c and d is approximately quadratic. That is, a homoclinic orbit to the focus-focus \mathbf{q} exists whenever c and d satisfy $d \approx 0.0437881c^2 - 0.0016566c + 1.2656854$, for $0 \leq c \leq 1$; the root mean square error of this approximation is $e = 6.8 \times 10^{-5}$. In particular, the computed segment of the curve h_q is located in the half-space

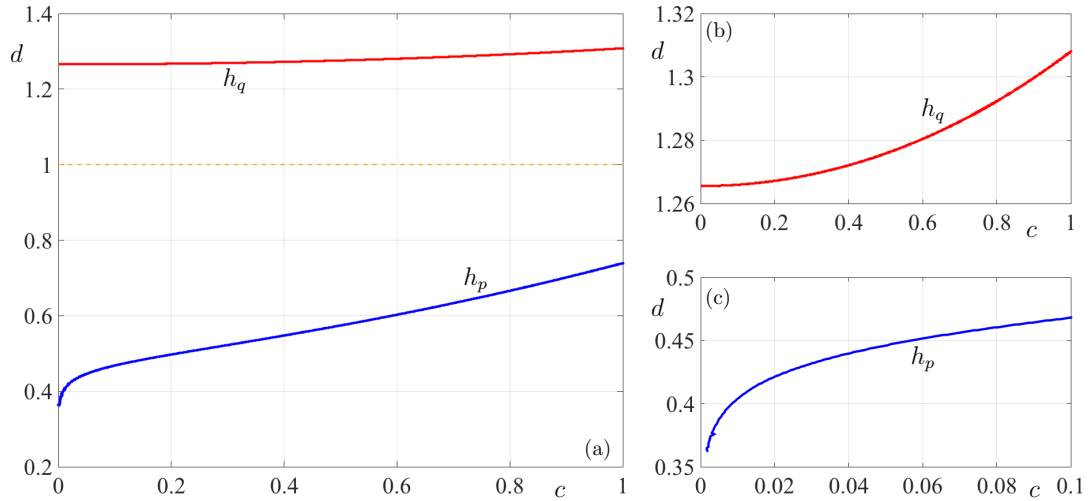


FIGURE 19. The homoclinic bifurcation curves h_p and h_q in the (c, d) -plane in panel (a). Panels (b) and (c) show enlargements near the curves h_q and h_p , respectively (the apparently different shape of each curve is due to the different scales in each plot). Parameter $m = 0.0463358$ and the other parameters are as in Figure 1.

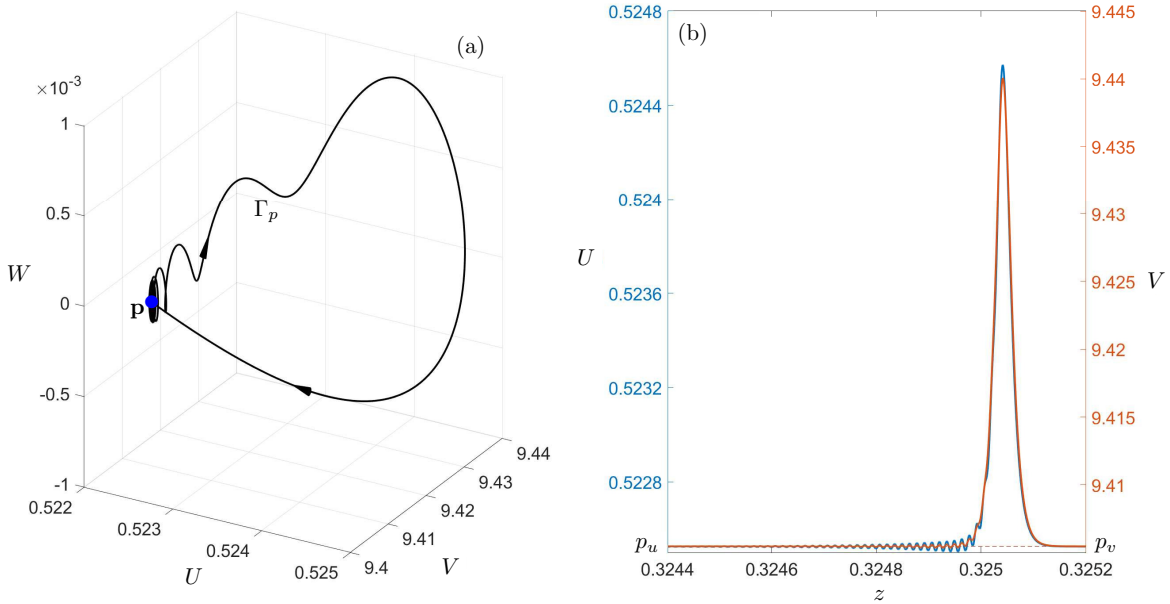


FIGURE 20. The homoclinic orbit Γ_p to \mathbf{p} , when $(c, d) = (0.0479321, 0.4449391)$ in panel (a) and its wave profile in panel (b). The other parameter values are as in Figure 19.

$d > 1$. Hence, this kind of pulse wave with small wave speed $c < 1$ occurs only if U propagates in a more efficient way than V . Moreover, the numerical evidence suggests that a pulse wave exists for every $c > 0$ arbitrarily small, i.e., there is no positive minimum value for the wave speed c . Indeed, the bifurcation curve h_q can be continued down to $c_{\min} = 0$ with $d_{\min} \approx 1.2656854$. (In particular, the value $d_{\min} > 0$ prevents (3) and (4) to become singular, unlike the case of h_p). In the limit as $c \rightarrow 0$, the resulting wave pulse corresponds to a stationary solution of (2) where both state variables U and V propagate with diffusion ratio $D_1/D_2 = d_{\min}$.

10. TRAVELING WAVES RESTRICTED TO INVARIANT PLANES

System (4) has two invariant planes given by

$$\Pi_U = \{(U, V, W, R) \in \mathbb{R}^4 : V = R = 0\},$$

and

$$\Pi_V = \{(U, V, W, R) \in \mathbb{R}^4 : U = W = 0\}.$$

Note that the origin $\mathbf{p}_0 \in \Pi_U \cap \Pi_V$. The restriction of (4) to Π_U is given by

$$X_U : \begin{cases} \frac{dU}{dz} = W, \\ \frac{dW}{dz} = \frac{1}{d} (cW - sU^2(U - m)(1 - U)). \end{cases} \quad (6)$$

System (6) has three equilibria: $\mathbf{0} = (0, 0)$, $(m, 0)$ and $(1, 0)$, which correspond to the restrictions of \mathbf{p}_0 , \mathbf{p}_m and \mathbf{p}_1 , respectively, to Π_U . The equilibrium $(m, 0)$ is a hyperbolic repeller and $(1, 0)$ is a hyperbolic saddle of (6). This result is a direct consequence of Hartman-Grobman theorem. Indeed, the linear part of (6) is given by

$$DX_U(U, W) = \begin{pmatrix} 0 & 1 \\ \frac{s}{d} (4U^3 - 3(m+1)U^2 + 2mU) & \frac{c}{d} \end{pmatrix}.$$

Therefore, evaluation of DX_U at $(m, 0)$ and $(1, 0)$ is given, respectively, by

$$DX_U(m, 0) = \begin{pmatrix} 0 & 1 \\ \frac{s}{d} m^2(m-1) & \frac{c}{d} \end{pmatrix}, \quad DX_U(1, 0) = \begin{pmatrix} 0 & 1 \\ \frac{s}{d} (1-m) & \frac{c}{d} \end{pmatrix}.$$

Furthermore, the eigenvalues of $DX_U(m, 0)$ and $DX_U(1, 0)$ are given, respectively, by

$$\lambda_{\pm}^m = \frac{c \pm \sqrt{c^2 - 4sdm^2(1-m)}}{2d}, \quad \lambda_{\pm}^1 = \frac{c \pm \sqrt{c^2 + 4sd(1-m)}}{2d}.$$

Since $0 < m < 1$, then we have $c^2 - 4sdm^2(1-m) < c^2$. Therefore, $\text{Re}(\lambda_{\pm}^m) > 0$ and, hence, this proves that $(m, 0)$ is a repeller. On the other hand, note that $c^2 + 4sd(1-m) > c^2$, so $\lambda_-^1 < 0 < \lambda_+^1$. Thus, $(1, 0)$ is a saddle.

In the case of the origin $(0, 0)$ of (6), we have

$$DX_U(\mathbf{0}) = \begin{pmatrix} 0 & 1 \\ 0 & \frac{c}{d} \end{pmatrix},$$

with associated eigenvalues $\lambda_1^0 = 0$, and $\lambda_2^0 = c/d > 0$. Hence, $\mathbf{0}$ is a non-hyperbolic equilibrium. The eigenvectors of $DX_U(\mathbf{0})$ associated with λ_1^0 and λ_2^0 are $v_1^0 = (1, 0)^T$ and $v_2^0 = (c, d)^T$, respectively. According to the centre manifold theorem [21], the origin of (6) has a one-dimensional local centre manifold $W_{\text{loc}}^c(\mathbf{0})$ which is tangent to v_1^0 at $\mathbf{0}$. This implies that $W_{\text{loc}}^c(\mathbf{0})$ can be represented locally as

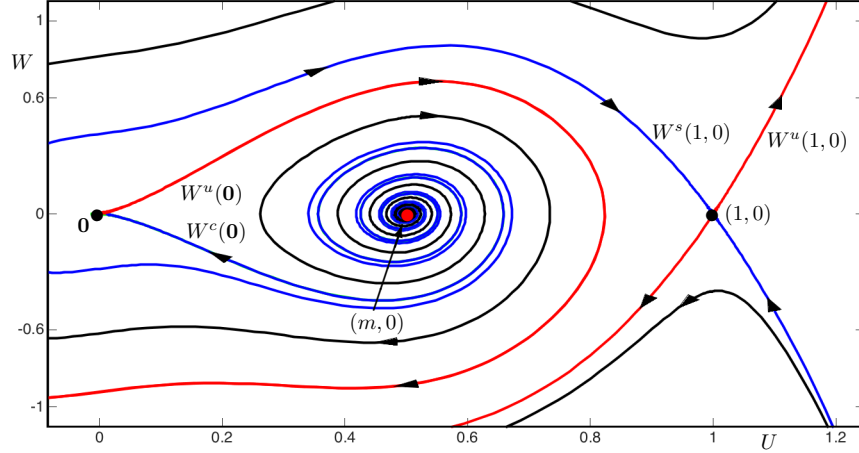


FIGURE 21. The centre manifold $W^c(\mathbf{0})$ extends itself (for $z < 0$) along the flow of (6) and forms a heteroclinic connection to $(m, 0)$. This corresponds to a wave front in (2). Parameter values in (6) are $(c, d, m, s) = (1, 2.4, 0.5, 100)$.

the graph of a function $W = W(U)$ that satisfies $W(0) = W'(0) = 0$ (for further details, see [30]). By taking the Taylor series expansion of this function around $U = 0$, we have

$$W(U) = \sum_{k=2}^r a_k U^k + \mathcal{O}(U^{r+1}),$$

where the coefficients $a_k \in \mathbb{R}$, and $\mathcal{O}(U^{r+1})$ are terms of order $r + 1$ and higher of the Taylor series of $W(U)$. Here, the coefficients a_k are determined by substitution of $W = W(U)$ into (6). Thus, after some calculations, we obtain

$$W(U) = -\frac{ms}{c}U^2 + \mathcal{O}(U^3).$$

If we restrict (6) to $W_{\text{loc}}^c(\mathbf{0})$, we obtain the scalar differential equation

$$U' = W(U) = -\frac{ms}{c}U^2 + \mathcal{O}(U^3).$$

Then, for $U > 0$ small enough, we have that $U' < 0$. Therefore, $\mathbf{0}$ is a local attractor in $W_{\text{loc}}^c(\mathbf{0})$. Since $\lambda_2^0 > 0$, it follows that $\mathbf{0}$ is a non-hyperbolic saddle point of (6).

Figure 21 shows the phase portrait of (6). The global centre manifold $W^c(\mathbf{0})$ extends itself (for $z < 0$) along the flow of (6) and forms a heteroclinic connection to $(m, 0)$. This corresponds to a wave front in (2) in which $v \equiv 0$ and $u \rightarrow 0$ as $t \rightarrow \infty$. Moreover, since $W^u(m, 0)$ is a two-dimensional unstable manifold, the intersection along $W^c(\mathbf{0}) \cap W^u(m, 0)$ is transversal. It follows that the associated wave front persists under small parameter variations. Notice that, under suitable parameter perturbations, the manifolds $W^u(\mathbf{0})$ and $W^s(1, 0)$ may come to intersect along a second heteroclinic orbit from $(0, 0)$ to $(1, 0)$. Since this manifold intersection is non-transversal, the resulting heteroclinic orbit is structurally unstable, i.e., it might be broken under small parameter variation. However, the front itself could still persist in the PDE (2), but perhaps with a slightly adjusted speed c .

Finally, a similar analysis of (4) restricted to the invariant plane Π_V reveals that there are either no homoclinic, heteroclinic orbits nor limit cycles with non-negative V -coordinates in Π_V .

TABLE 1. Summary of the main traveling wave solutions.

Wave type	Region in (m, d) plane	Orbit in phase space
Type A wave pulse	Bifurcation curve h_q	Focus-focus homoclinic orbit Γ_q
Type B wave pulse	Bifurcation curve h_p	Saddle-focus homoclinic orbit Γ_p
Type C wave pulse	Neighborhoods of h_q	Focus-focus 2-homoclinic orbit Γ_q^2
Type D wave pulse	Neighborhoods of h_p	Saddle-focus 2-homoclinic orbit Γ_p^2
Type E wave pulse	Neighborhoods of h_p	Saddle-focus 4-homoclinic orbit Γ_p^4
Type F wave pulse	Neighborhoods of h_q	Focus-focus 3-homoclinic orbit Γ_q^3
Type A wave front	Region I	Heteroclinic orbit from \mathbf{q} to \mathbf{p} $\Gamma_{q,p}$
Type B wave front	h_q and Regions III, IV, V	Heteroclinic orbit from \mathbf{p} to \mathbf{q} $\Gamma_{p,q}$
Type A wave train	Regions II, III, IV, V and VI	Limit cycle, Γ
Type B wave train	Regions III and V	2-turns limit cycle, Γ^2
Type C wave train	Region III	4-turns limit cycle, Γ^4
Type D wave train	Region III	8-turns limit cycle, Γ^8

11. DISCUSSION

We have investigated a diffusive process in a qualitative model (1) inspired by some minimal mathematical ingredients of a rescaled predator-prey interaction from [5]. Our goal was to undertake a systematic identification of traveling waves that may be encountered when the kinetic terms —based on those in [5]— are stated in their most elementary form. In particular, the analysis was performed searching for traveling wave solutions with strictly non-negative (u, v) coordinates. While the considered system may rise some questions regarding its interpretability, this “prototype model” may be understood in the same spirit as investigating a sort of topological normal form: namely, if the kinetic terms are presented in their most reduced (and yet mathematically meaningful) form, what can one expect in terms of spatiotemporal behavior if diffusion is taken care of. Nevertheless, upon taking these observations into consideration, we opted not to call variables u and v as “prey” and “predator”, respectively, in order to avoid misleading conclusions and interpretations of our results.

In (1) the three main types of traveling waves we were looking for appear: wave pulses, wave fronts, and wave trains. Table 1 shows a list of all the traveling waves exposed throughout this paper, together with the regions of the bifurcation diagram in Figure 4 where they can be found. We highlight that we made this table according to the obtained information, and the mentioned regions may not be the only ones where the given traveling waves can be found. Regarding the diffusion process, we found the condition $d > 1$ favors the presence of chaotic orbits in the traveling frame, i.e., the associated ODE system (4) is more likely to be chaotic when D_u is higher than D_v . Specifically, we can find chaos when (m, d) lies in the neighborhood of the h_p , h_q curves (homoclinic chaos) and the Neimark-Sacker curve NS in the bifurcation diagram; see also the discussion in Figure 5.

It is relevant to remember that there are regions where two or more types of traveling waves exist simultaneously. For example, if (m, d) is in the intersection between h_q and h_p , then there are two homoclinic orbits, Γ_q and Γ_p . Furthermore, let us remember that Γ^2 is branched from Γ when (m, d) crosses the period-doubling curve PD from region II to III. However, Γ does not disappear after this event. In fact, after the successive period doubling bifurcations, a large number of wave trains may be found together in the phase portrait of system (4). Finally, we should recall that when $(m, d) \approx (0.0463358, 1.3080156) \in h_q$, there is a family of heteroclinic orbits, which go from \mathbf{p} to \mathbf{q} . These arise from a transverse intersection between $W^u(\mathbf{p})$ and $W^s(\mathbf{q})$, which indicates that these solutions are robust under small changes of parameter values.

A relevant fact regarding the homoclinic orbit Γ_q is that it presents Shilnikov focus-focus homoclinic chaos in a concrete model vector field. Indeed, most of the studies about this bifurcation have been carried out (so far) only theoretically [19, 52]. Moreover, as far as we know, this work represents the first example of the actual computation of a global two-dimensional invariant manifold involved in a focus-focus homoclinic bifurcation in \mathbb{R}^4 .

We also performed a thorough search for traveling waves connecting stationary states with $V = 0$ to invariant objects with $U, V > 0$ in each parameter region in Figure 4 (In the particular case of p_m , we chose $c = 10$ in order to ensure its eigenvalues are real). This procedure involved the computation of 3D and 4D unstable manifolds of equilibria p_1 and p_m , respectively, following the scheme from [11]. Unfortunately, all the computed orbits have negative (U, V) coordinates for some $z > 0$ and, hence, did not match our initial criterium of non-negativity.

While the amplitude of the solutions we found may be rather small, it is important to emphasize that our results are qualitative; that is, our aim was not to present specifically quantitative features of the predator-prey interaction on which the system is based, but to show what kind of dynamical behavior one may hope to find, either theoretically or numerically. That said, the amplitude of the oscillations varies in markedly different scales for the rescaled variables, and variations in V are much more pronounced than those of U for pulses, fronts and trains. This difference in amplitudes can be explained by paying attention to the following observations: (i) quantities u and v spatially spread at distinct rates. This rate difference provides that the low-diffusivity variable promotes a heterogeneous aggregation of both variables along the domain; in consequence, both traveling-wave profiles propagate in a spatially non-homogenous shape, regardless of $d < 1$ or $d > 1$; (ii) the ratio in the original variables u/v prevails as both amplitudes are of the same order in any escenarios here considered; (iii) upon integrating system (2) along finite spatial domain, and assuming uniform convergence in time, we obtain that solutions satisfy formulae:

$$(7a) \quad \int_{-L}^L [su(u-m)(1-u)(u+v) - auv] dx = \frac{d\mathcal{B}_1}{dt},$$

$$(7b) \quad \int_{-L}^L [buw - gv(u+v)] dx = \frac{d\mathcal{B}_2}{dt},$$

where the total ‘‘masses’’ are given by $\mathcal{B}_1(t) = \int_{-L}^L u dx$ and $\mathcal{B}_2(t) = \int_{-L}^L v dx$, regardless of whether the boundary conditions for u_x and v_x vanish or cancel out each other at $x = \pm L$. Moreover, once we define the weighted total mass by $\mathcal{B}(t) := b\mathcal{B}_1(t) + a\mathcal{B}_2(t)$, from (7), we obtain formula

$$(8) \quad \int_{-L}^L [bsu(u-m)(1-u) - agv](u+v) dx = \frac{d\mathcal{B}}{dt}.$$

Upon taking into account $L \gg 1$, we get traveling-wave solutions of (2), which are characterized by having profiles that keep their shape over time. Now, we consider a moving interval-frame $\mathcal{J} = [-L - ct, L - ct]$, which ‘‘runs alongside’’ the traveling profiles with the same speed $c \geq 0$. In so doing, integral in the left-hand side term of (8) over \mathcal{J} is constant for all $t \geq 0$. That is, since traveling-wave profiles displacement only changes their position in time, the weighted total mass traveling speed is therefore conserved, i.e. $d\mathcal{B}/dt \equiv \mathcal{C}_0$, where \mathcal{C}_0 is constant. Thus, as $u + v \geq 0$ for all $|x| \leq L$, the total masses of the two variables follow a conservation-like property for traveling-wave solutions. Namely, as the wave variable $z = x + ct$ corresponds to a spatial translation for $t \geq 0$, variable amplitudes balance each other to satisfy identity (8) for a constant weighted total mass rate of change \mathcal{C}_0 .

It is interesting to note that identities in (7) are also satisfied for stationary solutions; that is, upon setting $u_t = v_t = 0$, we have relation (8) with $d\mathcal{B}/dt \equiv 0$, when homogeneous Neumann boundary

conditions are in place. Similar identities are obtained for Dirichlet, periodic and mixed-type boundary conditions, as well. In addition, this model may be able to develop diffusion-driven instabilities by means of Turing bifurcations. Nonetheless, in order to perform such an analysis, a stationary spatial pattern setting must be taken into account.

Finally, we studied the stability of every wave solution we detected, and we found that each of them is unstable. We followed the approach from [8, 44, 45]: In a general PDE of the form

$$\mathbf{u}_t = \mathbf{f}(\mathbf{u}) + D \mathbf{u}_{xx},$$

traveling waves are functions $\mathbf{U}(z)$, where $z = x + ct$. In particular, defining the new pair of variables $(\xi, t) = (x + ct, t)$, we have that

$$\mathbf{u}_t = c \mathbf{u}_\xi + \mathbf{u}_t, \quad \mathbf{u}_{xx} = \mathbf{u}_{\xi\xi}.$$

This implies that the system can be written as

$$\mathbf{u}_t = -c \mathbf{u}_\xi + \mathbf{f}(\mathbf{u}) + D \mathbf{u}_{\xi\xi}. \quad (9)$$

In our case, $\mathbf{u} = (u, v)$, \mathbf{f} stands for the reaction part of (2), and $D = \begin{pmatrix} d & 0 \\ 0 & 1 \end{pmatrix}$. Notice that when $\mathbf{u}_t = \mathbf{0}$ in (9) we recover the ODE system (3) for traveling waves. This means that traveling waves are a stationary solution of (9). We then linearized it and evaluated the traveling waves we found. In particular, we obtained the spectral stability by numerically computing the ten eigenvalues with the largest real part of the Jacobian matrix of (9) and noticed that (in every run) the spectrum obtained had at least one of them being positive. We also tried with different mesh refinements and the results were consistent.

REFERENCES

- [1] Valentin S Afraimovich, Sergey V Gonchenko, Lev M Lerman, Andrey L Shilnikov, and Dmitry V Turaev. Scientific heritage of I. P. Shilnikov. *Regular and Chaotic Dynamics*, 19(4):435–460, 2014.
- [2] P. Aguirre, E. Doedel, B. Krauskopf, and H. M. Osinga. Investigating the consequences of global bifurcations for two-dimensional invariant manifolds of vector fields. *Discr. Cont. Dynam. Syst.*, 29(4):1309–1344, 2010.
- [3] P. Aguirre, B. Krauskopf, and H. M. Osinga. Global invariant manifolds near homoclinic orbits to a real saddle: (non) orientability and flip bifurcation. *SIAM J. Appl. Dynam. Syst.*, 12(4):1803–1846, 2013.
- [4] Pablo Aguirre. Bifurcations of two-dimensional global invariant manifolds near a noncentral saddle-node homoclinic orbit. *SIAM Journal on Applied Dynamical Systems*, 14(3):1600–1643, 2015.
- [5] Pablo Aguirre, José D Flores, and Eduardo González-Olivares. Bifurcations and global dynamics in a predator–prey model with a strong allee effect on the prey, and a ratio-dependent functional response. *Nonlinear Analysis: Real World Applications*, 16:235–249, 2014.
- [6] Pablo Aguirre, Bernd Krauskopf, and Hinke M Osinga. Global invariant manifolds near a shilnikov homoclinic bifurcation. *Journal of Computational Dynamics*, 1(1):1–38, 2014.
- [7] L. A. Belyakov. Bifurcation of systems with homoclinic curve of a saddle-focus with saddle quantity zero. *Mat. Zam.*, 36:681–689, 1984.
- [8] Víctor Breña Medina, Alan R Champneys, C Grierson, and Michael Jeffrey Ward. Mathematical modeling of plant root hair initiation: Dynamics of localized patches. *SIAM Journal on Applied Dynamical Systems*, 13(1):210–248, 2014.
- [9] Víctor Breña-Medina and Alan Champneys. Subcritical turing bifurcation and the morphogenesis of localized patterns. *Physical Review E*, 90(3):032923, 2014.
- [10] Alan R Champneys, Yu A Kuznetsov, and Björn Sandstede. A numerical toolbox for homoclinic bifurcation analysis. *International Journal of Bifurcation and Chaos*, 6(05):867–887, 1996.
- [11] Dana Contreras-Julio, Pablo Aguirre, José Mujica, and Olga Vasilieva. Finding strategies to regulate propagation and containment of dengue via invariant manifold analysis. *SIAM Journal on Applied Dynamical Systems*, 19(2):1392–1437, 2020.
- [12] A. Dhooge, W. Govaerts, Yu. A. Kuznetsov, H. G.E. Meijer, and B. Sautois. New features of the software matcont for bifurcation analysis of dynamical systems. *Mathematical and Computer Modelling of Dynamical Systems*, 14(2):147–175, 2008.

- [13] E. J. Doedel. Lecture notes on numerical analysis of nonlinear equations. In *Numerical Continuation Methods for Dynamical Systems*, pages 1–49. Springer, 2007.
- [14] Eusebius J Doedel, Thomas F Fairgrieve, Björn Sandstede, Alan R Champneys, Yuri A Kuznetsov, and Xianjun Wang. *AUTO-07P: Continuation and bifurcation software for ordinary differential equations*, 2007.
- [15] Steven R Dunbar. Traveling waves in diffusive predator–prey equations: periodic orbits and point-to-periodic heteroclinic orbits. *SIAM Journal on Applied Mathematics*, 46(6):1057–1078, 1986.
- [16] G. B. Ermentrout and Terman D. H. *Mathematical Foundations of Neuroscience*. Springer, New York, NY, 2010.
- [17] G. B. Ermentrout and N. Kopell. Parabolic bursting in an excitable system coupled with a slow oscillation. *SIAM J. Appl. Math.*, 46(2):233–253, 1986.
- [18] N. Fenichel. Geometric singular perturbation theory for ordinary differential equations. *J. Differ. Equations*, 31(1):53–98, 1979.
- [19] AC Fowler and CT Sparrow. Bifocal homoclinic orbits in four dimensions. *Nonlinearity*, 4(4):1159–1182, 1991.
- [20] J. Guckenheimer, B. Krauskopf, H. M. Osinga, and B. Sandstede. Invariant manifolds and global bifurcations. *Chaos*, 25(9):097604, 2015.
- [21] John Guckenheimer and Philip Holmes. *Nonlinear oscillations, dynamical systems, and bifurcations of vector fields*, volume 42. Springer Science & Business Media, 2013.
- [22] Morris W. Hirsch. *Differential Topology*, volume 33 of *Graduate Texts in Mathematics*. Springer, 1976.
- [23] Ale Jan Homburg and Björn Sandstede. Homoclinic and heteroclinic bifurcations in vector fields. *Handbook of Dynamical Systems*, 3:379–524, 2010.
- [24] Cheng-Hsiung Hsu, Chi-Ru Yang, Ting-Hui Yang, and Tzi-Sheng Yang. Existence of traveling wave solutions for diffusive predator–prey type systems. *Journal of Differential Equations*, 252(4):3040–3075, 2012.
- [25] Jianhua Huang, Gang Lu, and Shigui Ruan. Existence of traveling wave solutions in a diffusive predator-prey model. *Journal of Mathematical Biology*, 46(2):132–152, 2003.
- [26] E.M. Izhikevich. Simple model of spiking neurons. *IEEE Transactions on Neural Networks*, 14(6):1569–1572, 2003.
- [27] B. Krauskopf and T. Rieß. A Lin’s method approach to finding and continuing heteroclinic connections involving periodic orbits. *Nonlinearity*, 21(8):1655, 2008.
- [28] Bernd Krauskopf and Hinke M Osinga. Computing invariant manifolds via the continuation of orbit segments. In *Numerical Continuation Methods for Dynamical Systems*, pages 117–154. Springer, 2007.
- [29] Bernd Krauskopf, Hinke M Osinga, Eusebius J Doedel, Michael E Henderson, John Guckenheimer, Alexander Vladimirovsky, Michael Dellnitz, and Oliver Junge. A survey of methods for computing (un) stable manifolds of vector fields. In *Modeling And Computations In Dynamical Systems: In Commemoration of the 100th Anniversary of the Birth of John von Neumann*, pages 67–95. World Scientific, 2006.
- [30] Yuri A Kuznetsov. *Elements of applied bifurcation theory*, volume 112. Springer Science & Business Media, 2013.
- [31] M.A. Lewis and B. Li. Spreading Speed, Traveling Waves, and Minimal Domain Size in Impulsive Reaction–Diffusion Models. *Bull. Math. Biol.*, 74:2383–2402, 2012.
- [32] Huiru Li and Haibin Xiao. Traveling wave solutions for diffusive predator–prey type systems with nonlinear density dependence. *Computers & mathematics with applications*, 74(10):2221–2230, 2017.
- [33] Xiaobiao Lin, Peixuan Weng, and Chufen Wu. Traveling wave solutions for a predator–prey system with sigmoidal response function. *Journal of Dynamics and Differential Equations*, 23(4):903–921, 2011.
- [34] Dolnik M., Zhabotinsky A.M., A.B. Rovinsky, and Epstein I.R. Spatio-temporal patterns in a reaction-diffusion system with wave instability. *Chem. Eng. Sci.*, 55:223–231, 2000.
- [35] K. Manna, S. Pal, and M. Banerjee. Analytical and numerical detection of traveling wave and wave-train solutions in a prey–predator model with weak allee effect. *Nonlinear Dyn.*, 100:2989–3006, 2020.
- [36] J. Mujica, B. Krauskopf, and H. M. Osinga. A Lin’s method approach for detecting all canard orbits arising from a folded node. *J. Comput. Dyn.*, 4:143–165, 2017.
- [37] J. Mujica, B. Krauskopf, and H. M. Osinga. Tangencies between global invariant manifolds and slow manifolds near a singular Hopf bifurcation. *SIAM J. Appl. Dyn. Syst.*, 17:395–1431, 2018.
- [38] James D Murray. *Mathematical biology: I. An introduction*, volume 17. Springer, 2000.
- [39] James D Murray. *Mathematical biology II: Spatial models and biomedical applications*, volume 18. Springer, 2001.
- [40] Hinke M Osinga. Two-dimensional invariant manifolds in four-dimensional dynamical systems. *Computers & Graphics*, 29(2):289–297, 2005.
- [41] IM Ovsyannikov and LP Shil’nikov. Systems with a homoclinic curve of multidimensional saddle-focus type, and spiral chaos. *Mathematics of the USSR-Sbornik*, 73(2):415–443, 1992.
- [42] C. M. Postlethwaite and A. M. Rucklidge. A trio of heteroclinic bifurcations arising from a model of spatially-extended Rock-Paper-Scissors. *Nonlinearity*, 32(4):1375–1407, 2019.
- [43] Björn Sandstede. Stability of n-fronts bifurcating from a twisted heteroclinic loop and an application to the Fitzhugh–Nagumo equation. *SIAM Journal on Mathematical Analysis*, 29(1):183–207, 1998.

- [44] Björn Sandstede. Stability of travelling waves. In *Handbook of dynamical systems*, volume 2, pages 983–1055. Elsevier, 2002.
- [45] Björn Sandstede and Arnd Scheel. On the stability of periodic travelling waves with large spatial period. *Journal of Differential Equations*, 172(1):134–188, 2001.
- [46] Jonathan A Sherratt and Matthew J Smith. Periodic travelling waves in cyclic populations: field studies and reaction–diffusion models. *Journal of the Royal Society Interface*, 5(22):483–505, 2008.
- [47] A Shilnikov and M Kolomiets. Methods of the qualitative theory for the Hindmarsh-Rose model: A case study. a tutorial. *International Journal of Bifurcation and Chaos*, 18(8):2141–2168, 2008.
- [48] L. P. Shilnikov. A case of the existence of a countable number of periodic orbits. *Sov. Math. Dokl.*, 6:163–166, 1965.
- [49] L. P. Shilnikov. A contribution to the problem of the structure of an extended neighborhood of a rough state to a saddle-focus type. *Math. USSR-Sb*, 10:91–102, 1970.
- [50] L. P. Shilnikov, A. L. Shilnikov, D. V. Turaev and L. Chua. *Methods of Qualitative Theory in Nonlinear Dynamics. Part II*. World Scientific Series on Nonlinear Science, Series A, Vol. 5, 2001.
- [51] L. T. Takahashi, N. A. Maidana, W. C. Ferreira, P. Pulino, and H. M. Yang. Mathematical models for the Aedes aegypti dispersal dynamics: travelling waves by wing and wind. *Bull. Math. Biol.*, 67(3):509–528, 2005.
- [52] Stephen Wiggins. *Global Bifurcations and Chaos: Analytical Methods*, volume 73. Springer Science & Business Media, 2013.
- [53] Xiujuan Wu, Yong Luo, and Yizheng Hu. Traveling waves in a diffusive predator-prey model incorporating a prey refuge. In *Abstract and Applied Analysis*, volume 2014. Hindawi, 2014.
- [54] W. M. S Yamashita, L. T. Takahashi, and G. Chapiro. Traveling wave solutions for the dispersive models describing population dynamics of Aedes aegypti. *Math. Comput. Simulat.*, 146:90–99, 2018.

*DEPARTMENT OF ENGINEERING MATHEMATICS, UNIVERSITY OF BRISTOL, BRISTOL BS8 1TW, UNITED KINGDOM.
Email address: `rt20469@bristol.ac.uk`

**DEPARTAMENTO DE MATEMÁTICA, UNIVERSIDAD TÉCNICA FEDERICO SANTA MARÍA, CASILLA 110-V, VALPARAÍSO, CHILE.
Email address: `pablo.aguirre@usm.cl`

†DEPARTMENT OF MATHEMATICS, ITAM, RÍO HONDO 1, CIUDAD DE MÉXICO 01080, MÉXICO.
Email address: `victor.brena@itam.mx`